



Modeling of heat transfer, fluid flow, and weld pool dynamics during keyhole laser welding of 316 LN stainless steel using hybrid conical-cylindrical heat source

Anoop Karaniath Unni¹ · Vasudevan Muthukumar^{1,2}

Received: 22 October 2021 / Accepted: 10 August 2022 / Published online: 15 September 2022
© The Author(s), under exclusive licence to Springer-Verlag London Ltd., part of Springer Nature 2022

Abstract

This study ascertains a three-dimensional (3D) numerical modeling employing hybrid conical-cylindrical heat source concerning the heat transfer, molten fluid flow weld pool dynamics, and cooling rate phenomena associated with the laser weld pool of 316 LN stainless steel (SS) by computational fluid dynamics. The heat source interprets the transmission of laser energy to the substrate by accounting for recoil pressure and surface tension effect using the multiphase flow modeling. The impact of laser power for a constant welding speed on the penetration depth is predicted to select an optimized laser energy input to carry out full penetration laser welding experiment. The model pictures the depth of penetration, temperature distribution, velocity field, and weld pool flow pattern and keyhole behavior for the optimized welding condition. Non-dimensional heat transfer entities such as Peclet and Marangoni numbers are also assessed that provide insight related to the thermal-fluid flow mechanism and final weld fusion zone attributes of the 316 LN SS laser weld. The simulated model agrees well with the experimentally achieved full penetration laser weld giving fair concordance with the weld bead dimensions and thermocouple measurements. The model has been used to calculate the secondary dendritic arm spacing in the fusion zone. Calculated values were in agreement with the measured values. The numerical outcomes recognize that the hybrid conical-cylindrical heat source model is well suited for predicting weld peak temperature, weld pool velocity, weld pool dynamics, weld pool shape, and cooling rate for the laser welding of 316 LN SS.

Keywords Computational fluid dynamics (CFD) · Hybrid conical-cylindrical heat source · Volume of fluid (VOF) · Keyhole laser welding · Non-dimensional number · AISI 316 LN SS

1 Introduction

Austenitic stainless steels are famed for their innate corrosion resistance, making them ideal for use in various large-scale industries, including the petrochemicals, gas, food processing, and power generation. The austenitic steel grade 316 LN medium and thick plates are generally recommended as the building material for structural and critical components of nuclear reactors due to their superior strength and

intergranular corrosion resistance [1, 2]. The weld joint of 316 LN SS generated using different fusion welding techniques induces excessive heat input and thermal deformation during the fabrication process if adequate settings are not made. These issues are reduced considerably during the laser welding process resulting in superior weld quality and performance during the service life. The ability to deliver low heat input combined with high welding speed, restricted heat-affected zone, and deep penetration welds has been the attraction of the laser welding process explained by Bachmann et al. [3]. Researchers have done numerous process parameter optimization studies related to laser welding and keyhole physics to achieve high-quality weld joints. But still, comprehending the molten pool characteristics and dynamics of the keyhole in the presence of surface-active element (sulfur) for different steel grades is essential, and no experiments can adequately complement this knowledge in terms of the effect on convection pattern. As a result, numerical modeling studies were

✉ Vasudevan Muthukumar
dev@igcar.gov.in

¹ Homi Bhabha National Institute, Mumbai, India

² Materials Development and Technology Division, Materials Engineering Group, Metallurgy and Materials Group, Indira Gandhi Centre for Atomic Research, Kalpakkam, Tamil Nadu 603102, India

performed to assess the effectiveness of the laser process and the different complexities involved.

Mackwood and Crafer [4] reviewed about thermo-mechanical modeling using the finite element method (FEM) and the finite volume method. The solution method can be adopted for accurate predictions of thermal distribution, heat and fluid flow in the weld, alloy concentration, weld plastic strain, residual stress, and distortion. Xia et al. [5] developed a 3D FEM model for predicting weld bead geometry during fiber laser welding giving satisfactory results with the experimental trials. However, the calculation ignored convective flow and free surface evolution. Compared to FEM software such as Abaqus and SYSWELD, the benefit of having CFD simulation is superior in terms of technique, heat transport, and model accuracy validated using temperature data and weld fusion zone profile. With CFD modeling, a complete description of the molten pool flow, weld and heat-affected zone geometries, the effect of surface-active elements, solidification pattern, and investigation of convection mechanism for welding processes are prominent [6].

The preliminary task in any welding simulation is to establish an effective heat source for delivering the laser power to melt the substrate and generate temperature profile. Many types of research and reviews on heat source modeling were conducted. The first generation of heat sources employed for welding simulation considered a point, line, or surface distribution [7, 8]. Numerical models based on first-generation heat sources were developed and described by many authors [9–11]. However, various assumptions and simplifications in the model were added, such as ignoring fluid movement, assuming a flat weld top surface, and enhancing the material's thermal conductivity and specific heat. Later, with the improvement and advancement of computer technology, researchers could incorporate complex and multiphysics phenomena in molding a proper heat source model for performing both thermal and fluid flow computation for medium and thick plates. As a response, volumetric 3D heat distribution was introduced replacing the line or surface heat sources. Different forms of volumetric heat source models for partial and complete penetration welding were created and modeled for different plate thicknesses. The Goldak double ellipsoidal model, volumetric Gaussian model, 3D conical model, the combination of cone and cylindrical heat sources, and rotary heat source models are few among them. The mathematical modeling of these heat sources has been extensively researched, modified, and adapted for various numerical studies based on experimentally determined weld pool geometry [12, 13]. Attar et al. [14] simulated dissimilar keyhole laser welding of copper and 304 SS and using six different heat source models and suggested volumetric double conical as the ideal heat source. A 3D FEM model using SYSWELD developed by

Tsirkas et al. [15] considered a moving conical heat source in order to predict weld temperature and weld distortion in AH36 butt-joint plate giving fair result with the experimental measurement. Shanmugam et al. [16] used 3D conical heat source for predicting weld bead dimension in 304 SS sheet employing SYSWELD code giving satisfactory result with experimental bead dimensions. Also, latent heat and heat loss boundary conditions were incorporated in the simulation yielding fair results. Li et al. [17] used rotary Gaussian laser heat source for understanding the mechanism of porosity generation and the model proved to be reliable. Jiang et al. [18] used the combination of double ellipsoid and rotary Gaussian heat source by proposing an integration method for laser welding parameter optimization in 316L SS. A similar combination of heat source was used to describe weld pool dynamics during laser welding of 5A06 aluminum alloy under sub atmospheric pressures [19]. The model was apt for deep penetration welds. Faraji et al. [20] presented the heat transfer and fluid flow calculation during hybrid laser-TIG welding of aluminum alloy. In this, a combined cone and cylindrical heat source model was formulated for laser source and the model was validated with experimental measurements achieving close agreement. Wang et al. [21] developed a 3D heat source model using volumetric Gaussian heat source. The model was apt for partial penetration in predicting transient temperature and weld pool formation in 304 SS sheet. Zhan et al. [22] developed heat source model resembling an hourglass-like shape for laser welding of 1060 steel and found that the heat source model is more consistent with experimental results. According to Chukkan et al. [23], the heat source model for laser welding adopting a conical with cylindrical shell exhibited reasonable agreement for the thermo-mechanical study of 316 L SS using SYSWELD. A similar heat source modeling work was performed by Evdokimov et al. [24] for laser welding of steel-aluminum lap joint. Both these investigations were based on finite element technique. Unni and Vasudevan [25] performed a CFD investigation on 316 LN SS using different heat source models to determine the best heat source. The outcome suggested that the combination of the conical and cylindrical model produced the best fit. Similarly, Artinov et al. [26] proposed an equivalent volumetric heat source model using COMSOL for calculating weld pool shape and temperature field. However, both studies ignored the effect of recoil pressure and molten pool calculation. The current study will employ hybrid conical-cylindrical heat source model using VOF method to investigate the heat transfer and fluid flow mechanism.

Welding of thick plates requires high laser power with an intensity of more than 10^6 W/cm². The interaction with the substrate at such power density creates intense vaporization leaving a depression with a long and narrow cavity in the surface known as a keyhole. The keyhole mode is an

essential phenomenon in laser welding for achieving deeper penetration. The art of keyhole creation has been studied by many researchers in developing numerical models to simulate laser welding processes. The simulation work by Lee et al. [27] demonstrated that keyhole is formed with the aid of recoil pressure displacing the molten melt, and surface tension and hydrodynamic pressure oppose the cavity formation. Rońda and Siwek [28] analyzed different stages of keyhole evolution by CFD, considering process parameters an essential function for forming the weld. Zhao et al. [29] used the volume of fluid (VOF) method to solve the multiphase problem by building a gas–liquid–solid-coupled model to see the evolution of keyhole. There was good agreement between experimental and numerical results. Feng et al. [30] developed a 3D model considering various body force term and phase changes for investigating weld penetration depth during laser welding of 304 SS. It was found that the weld penetration depth had severe effect on the temperature field and flow field. The current study develops a 3D multiphase model to track the free surface evolution of keyhole by applying the pressure boundary conditions adopting the hybrid conical-cylindrical heat source.

The study on the role of surfactants such as sulfur and oxygen in affecting the pattern of temperature distribution and fluid flow pattern has been explained by researchers. In welding, the temperature coefficient of surface tension (TCST) is of great importance since the strength and direction of weld pool flow are determined by its sign and magnitude. A low level of the surface-active element in the material can make the direction of fluid flow from the center towards the edges of the pool. The TCST is negative and pure metals normally exhibit such behavior, whereas the presence of high sulfur or oxygen in the material increases the surface tension at the center of the weld pool, changing the direction of fluid flow inward [31–33]. In this scenario, the TCST remains positive for most of the temperature range in the weld pool. Rai et al. [34] confirmed convective heat transfer as the main mechanism in 304 L SS by comparing the heat transfer calculation during laser welding of tantalum, Ti–6Al–4 V, 304L stainless steel, and vanadium. The TCST also affected the weld pool formation with pronounced spread for 304 L SS. Ribic et al. [35] developed a numerical model examining the role of sulfur and oxygen in the mild steel influencing the weld bead geometry and fluid flow. Likewise, the authors mentioned the importance of convection, signifying the presence of surface-active elements in understanding surface tension impelled flows.

For the weldability in austenitic stainless steel grades such as in type 304 and 316 plates of steel, a specified limit of sulfur has to be maintained in order to achieve good-quality weld. The quantity of sulfur in the substrate directly impacts the final weld bead attributes. Because too much sulfur can render the material unweldable, a safe level of

sulfur must be maintained. In this research, the amount of sulfur in the base metal was confirmed initially by chemical analysis and incorporated into the numerical model as a source term to study the impact of Marangoni convection on the weld bead characteristics.

Researchers are able to comprehend the underlying solidification and cooling trend attained from the predicted temperature and velocity data for a prescribed welding process parameter [36]. Geng et al. [37] summarized that the temperature gradient (G) and solidification rate (R) can be used to predict the grain morphology and size of grain structure based on the heat transfer and molten flow calculations. Similarly, solidification traits for laser welding of tantalum, Ti–6Al–4V, 304 SS, and vanadium were explained based on the numerical heat transfer and fluid flow calculation in the molten pool [34]. The cooling rate of the weld is mainly controlled by the amount of heat input and choice of a heat source, which reveals information related to the solidification features such as grain size and secondary dendrite arm spacing. Also, their impact on mechanical and metallurgical aspects of final weld joint is significant [38]. Together, they define the final weld mechanical behavior. Hence, the study of thermal-fluid flow can be extended to explore their impact on the solidification and cooling pattern in laser full penetration welding of 316 LN SS.

Experimental study performed by Zhao et al. [39] on laser welding has revealed unsteady and violent motion of free surface of the melt pool. Most of the early studies for computing the weld pool flows related to the assumption of laminar flow instead of the turbulence approach. However, numerical simulation studies of such flows using turbulent regime fail to predict the post-solidification weld pool shape and were found insufficient for matching the experimental results. Also the heat transfer calculations were found lower than the laminar model thus affecting the prediction of pool shape [40, 41]. Hence, in this study, laminar model may be used to avoid discrepancy between the experimental and simulation results.

These reports imply that the proper selection of the heat source model incorporating the Marangoni effect, recoil pressure, solidification, and cooling trend collectively govern the heat transfer and fluid flow, which define the final laser weld bead traits. The novelty in this work prevails in the foundation to understand the effect of heat transfer and molten flow using CFD multiphase modeling on laser weld pool development, keyhole evolution, and calculation of secondary dendritic arm spacing (SDAS) employing the optimized hybrid conical-cylindrical heat source for 316 LN SS. In our earlier work [25], we have used and compared the performance of five volumetric heat sources namely Goldak double ellipsoidal, 3D conical, 3D conical and cylindrical heat source, 3D volumetric Gaussian, and rotary Gaussian heat source model for simulating the weld pool for laser

welding of 316 LN SS for the first time. We have reported that a 3D conical-cylindrical model gave good conformance with the measured bead dimensions and thermal analysis data. The optimized heat source model is expected to simulate the actual weld bead shape and size, and predict weld pool temperature, molten flow velocity, keyhole profile, vapor velocity, and weld cooling rate fairly well for the laser welding of stainless steel. The model is capable to provide more insight on the weld pool evolution during laser welding. The model would also be used to calculate the SDAS across the fusion zone. Also, the hybrid conical-cylindrical heat source model is expected to be suitable for CFD simulation of laser welding of medium and large thickness plates.

The structure of the research article is framed into 5 sections commencing with the introduction part. Section 2 deals with the experimental work, techniques, and equipment employed. In Sect. 3, the governing equation is formulated, the heat source is modeled, and the computational domain's boundary conditions are established. Section 4 shows the numerical outcomes as well as a comparison with the experimental findings. Finally, the investigation is summarized in Sect. 5.

2 Material and experimental techniques

2.1 Material attributes

The austenitic steel grade of 316 LN SS plate with a thickness of 0.0055 m was used to carry out laser welding experiment. The specimen weld dimension was $0.30 \times 0.25 \times 0.0055 \text{ m}^3$. The chemical composition of 316 LN SS in wt% is C-0.02, N-0.110, Mn-1.73, Ni-12.13, Cr-16.91, Mo-2.48, S-0.008, Si-0.477, and P-0.025. Owing to high strength significantly with the addition of nitrogen and superior corrosion resistance properties at elevated temperatures, type 316 LN SS is remarkably employed in structural building materials and thermal-related applications in fast breeder test reactor facility.

2.2 Sulfur chemical analysis

In this study, CFD analysis was performed considering surface tension flow during laser welding of 316 LN SS. The amount of sulfur acting as surfactant influences the magnitude and direction of fluid flow due to the temperature coefficient of surface tension. For this, the quantity of sulfur present in the substrate ($0.03 \text{ m} \times 0.03 \text{ m}$ cut piece sample) was inspected prior to welding using optical emission spectrometer (OES-750 HITACHI, Germany) shown in Fig. 1 as



Fig. 1 Chemical analysis-optical emission spectrometer apparatus

per the ASTM E1086 standard. The sulfur in the base plate was confirmed to be 80 ppm after conducting the chemical analysis.

2.3 Continuous laser welding

The laser welding unit comprises a CO₂ gas laser system with slab geometry layout (ROFIN, Model: #DC-035, Germany), as illustrated in Fig. 2, operated either continuous or pulse wave mode. The maximum power density achieved in continuous laser welding is 3.5 kW. For attaining the final weld joint with the continuous wave, numerical trials have been performed to identify the laser power for achieving full penetration weld by keeping a constant welding current, and the optimized power is utilized for carrying out the welding. Table 1 lists the operating conditions employed in the welding process.

The plates were wiped with acetone to eliminate any surface contaminants present over them before the welding. During welding, helium was supplied through a nozzle of 2-mm diameter as shielding gas to avoid porosity formation and carry away the hot plume. Temperature distribution in the plate was recorded with type K TC during square butt welding. To measure the maximum temperature values at different locations away from the fusion zone, thermocouples (TCs) were positioned at 0.001 m, 0.002 m, 0.003 m, and 0.004 m. After welding, the

Fig. 2 Laser CO₂ welding machine **a** Laser welding experimental setup. **b** TC positions at 0.001 m, 0.0015 m, 0.002 m, and 0.004 m from weld center. **c** Laser square-butt welded joint

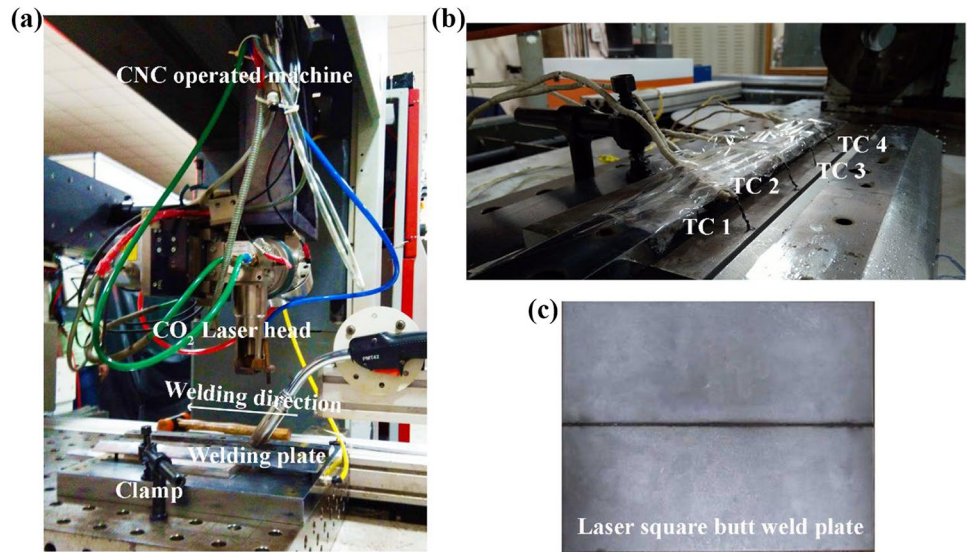


plate was taken for cutting and polishing to observe the weld macro section.

2.4 Metallographic analysis

For polishing and etching, a section of the weld sample was taken halfway across the weld. The sample was ground to a fine finish with emery sheets and polished with diamond paste to mirror finish. The sample was then electrolytically etched to disclose the weld fusion zone boundary and micro-structure using an equal measure of HNO₃ and H₂O. The top and bottom fusion zone widths were measured using a Zeiss stereomicroscope. Further, the SDAS was measured at

3 CFD modeling-numerical approach

3.1 Governing equations—mass, momentum, and energy

The numerical problem is solved using the finite-volume approach, built based on the Navier–Stokes equation and energy conservation. As stated below and expressed in the Cartesian coordinate system, the Navier–Stokes equations represent the continuity and X, Y, and Z momentum equations, respectively.

$$\frac{\partial \rho}{\partial t} + \frac{\partial(\rho u)}{\partial x} + \frac{\partial(\rho v)}{\partial y} + \frac{\partial(\rho w)}{\partial z} = 0 \tag{1}$$

$$\frac{\partial(\rho u)}{\partial t} + \frac{\partial(\rho uu)}{\partial x} + \frac{\partial(\rho vu)}{\partial y} + \frac{\partial(\rho wu)}{\partial z} = -\frac{\partial P}{\partial x} + \frac{\partial}{\partial x} \left(\mu \frac{\partial u}{\partial x} \right) + \frac{\partial}{\partial y} \left(\mu \frac{\partial u}{\partial y} \right) + \frac{\partial}{\partial z} \left(\mu \frac{\partial u}{\partial z} \right) + S_{xmom} \tag{2}$$

$$\frac{\partial(\rho v)}{\partial t} + \frac{\partial(\rho uv)}{\partial x} + \frac{\partial(\rho vv)}{\partial y} + \frac{\partial(\rho wv)}{\partial z} = -\frac{\partial P}{\partial y} + \frac{\partial}{\partial x} \left(\mu \frac{\partial v}{\partial x} \right) + \frac{\partial}{\partial y} \left(\mu \frac{\partial v}{\partial y} \right) + \frac{\partial}{\partial z} \left(\mu \frac{\partial v}{\partial z} \right) + S_{ymom} \tag{3}$$

$$\frac{\partial(\rho w)}{\partial t} + \frac{\partial(\rho uw)}{\partial x} + \frac{\partial(\rho vw)}{\partial y} + \frac{\partial(\rho ww)}{\partial z} = -\frac{\partial P}{\partial z} + \frac{\partial}{\partial x} \left(\mu \frac{\partial w}{\partial x} \right) + \frac{\partial}{\partial y} \left(\mu \frac{\partial w}{\partial y} \right) + \frac{\partial}{\partial z} \left(\mu \frac{\partial w}{\partial z} \right) + S_{zmom} \tag{4}$$

several locations in the fusion zone using the optical microscope, and the average value (μm) is reported in this study.

The energy equation is written in the form of enthalpy (*h*) and solved in the entire domain.

Table 1 CO₂ laser welding parameters

Parameters	Value
Laser power (kW)	3.3
Welding speed (m/s)	0.015
No of passes	1
Laser spot diameter (μm)	180
Wavelength (μm)	10.6
Defocussing length (mm)	0
Gas flow rate (L/min)	15

- Thermal conductivity, density, specific heat, and viscosity of the material are temperature dependent [32].
- Solidification and melting model are considered with enthalpy-porosity formulation for solid/liquid-phase change.
- Vaporization and recoil effect are incorporated considering latent heat of vaporization for liquid/vapor phase change.
- The amount of sulfur loss from the weld top surface is considered insignificant in the current study.
- The influence of the shielding gas on the molten pool dynamics is ignored.

$$\frac{\partial(\rho h)}{\partial t} + \frac{\partial(\rho u h)}{\partial x} + \frac{\partial(\rho v h)}{\partial y} + \frac{\partial(\rho w h)}{\partial z} = \frac{\partial}{\partial x} \left(k \frac{\partial T}{\partial x} \right) + \frac{\partial}{\partial y} \left(k \frac{\partial T}{\partial y} \right) + \frac{\partial}{\partial z} \left(k \frac{\partial T}{\partial z} \right) + S_{ene} \quad (5)$$

The pressure, density, viscosity, and body force source terms in the Navier–Stokes equation are given as P , ρ , μ , S_{xmom} , S_{ymom} , and S_{zmom} , respectively. Source terms consist of buoyancy, Marangoni force, and recoil pressure added to the momentum equation.

Here, the energy source term accounting for laser heating and melting is S_{ene} , k , and h are thermal conductivity and enthalpy of the substrate.

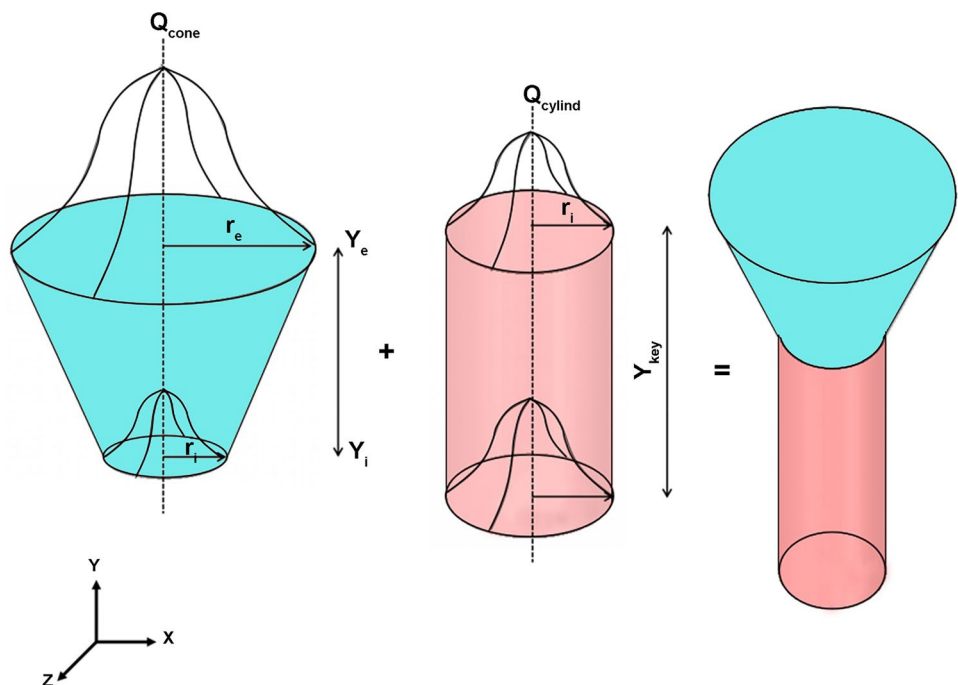
To simplify the model, the following assumptions listed down are used in the current study:

- The molten metal flow pattern inside the weld pool is laminar, Newtonian, and incompressible with buoyancy effect treated by Boussinesq assumption.

3.2 Modeling of the laser heat source by hybrid conical-cylindrical model

The laser heat energy is defined by a hybrid volumetric heat source delivering laser power to the workpiece to predict the welding temperature and keyhole formation. The hybrid heat source is the assemblage of volumetric heat sources of cone and cylinder with the cone at the top and cylinder at the bottom. The conical heat source model has maximum heat intensity at the top and decreases linearly along the thickness with minimum at the bottom radius. The top and bottom radii of the conical section are named as r_e and r_i with total cone height as $Y_e - Y_i$ as shown in Fig. 3. The cylindrical heat source model aids in demonstrating the

Fig. 3 Schematic of hybrid conical-cylindrical heat source model



keyhole depth formation (Y_{key}). The power distribution in the top cone (Q_{cone}) and bottom cylinder (Q_{cylind}) portion are given as [42]:

$$Q_{cone} = \frac{E_{upp} P_{las} \eta_{abs} f_{las}^2}{\pi (1 - e^{-3}) (Y_e - Y_i) (r_e^2 + r_e r_i + r_i^2)} \exp \left[\frac{-f_{las} r^2}{r_{las}^2} \right] \quad (6)$$

$$r_{las} = r_e - \frac{(r_e - r_i)(Y_e - Y)}{(Y_e - Y_i)} \quad (7)$$

$$Q_{cylind} = \frac{E_{low} P_{las} \eta_{abs}}{\pi r_i^2 Y_{key}} \quad (8)$$

The laser heat source parameters in Eqs. (6) and (8) are E_{upp} , E_{low} , η_{abs} , r_e , r_i , r_{las} , f_{las} , $Y_e - Y_i$, and Y_{key} . The above parameters were calibrated after fine tuning the values by comparing the experimental and predicted weld shape at laser powers of 2.5 kW and 3.5 kW to obtain the size and shape of weld pool. E_{upp} and E_{low} are the upper and lower energy factors taken as 0.4 and 0.6 respectively. The laser absorptivity (η_{abs}) is chosen as 0.6 [43]. The laser distribution parameter (f_{las}) is set as 3 and r_{las} is the effective laser radius given in Eq. (7). The top and bottom radii of cone were assumed as $r_e = 2r_{las}$ and $r_i = r_{las}$ respectively. Also, $Y_e - Y_i = 0.25Y_{key}$. Hence, the only parameter varying is laser power (P_{las}). The combined power distribution is embedded into the Fluent solver by writing an appropriate user-defined function (UDF) code using programming language C and compiled before calculation. The UDF is applied as a source term in the energy model to deliver the power during the calculation process.

3.3 Effect of TCST ($\partial\gamma/\partial T$) on sulfur content

Sahoo et al. [44] has determined the formula to obtain TCST for Fe–S-based system given in Eq. (9) by applying the factors of thermodynamic principle relevant to welding metallurgy. The sign and value of $\partial\gamma/\partial T$ depend upon the temperature and amount of sulfur present in the substrate. For pure metals, $\partial\gamma/\partial T$ tends to be negative, with surface tension flow occurring from a low concentration area (center) to a high concentration area (edge) as the temperature increase. In such a case, the molten pool shape is broader and shallower. Inversely, the increase in sulfur content can alter the sign of $\partial\gamma/\partial T$ resulting in the rise of surface tension, which causes the flow to be directed towards the center, making welds narrower and more profound.

$$\frac{\partial\gamma}{\partial T} = -A - R\Gamma_s \ln(1 + K_{seg} S_{cont}) - \frac{K_{seg} S_{cont}}{1 + K_{seg} S_{cont}} \frac{\Gamma_s (\Delta H^0)}{T} \quad (9)$$

$$K_{seg} = K_1 \exp\left(\frac{-\Delta H}{RT}\right) \quad (10)$$

where A is surface tension coefficient constant with the value of $4.3 \times 10^{-4} \text{ N m}^{-1} \text{ K}^{-1}$, R is the gas constant, ΔH^0 is the enthalpy of adsorption ($-166.2 \times 10^3 \text{ kJ (kgmol)}^{-1}$), Γ_s is the surface excess at saturation ($1.30 \times 10^{-8} \text{ kg mol m}^{-2}$), K_1 is the constant related to segregation (3.18×10^{-2}), K_{seg} is the equilibrium constant of segregation, and S_{cont} is the amount of sulfur content in ppm respectively. By varying the amount of S_{cont} in Eq. (9), TCST values are plotted against varying temperatures for the Fe–S binary system and the effect of TCST is considered a body source term during the calculation for S_{cont} (80 ppm) which is primarily responsible for Marangoni flow (Fig. 4).

3.4 Defining boundary conditions

For the current analysis, only half of the domain is considered owing to the geometrical symmetry to save computational time. The Cartesian coordinate system X , Y , and Z are represented in 3D and symmetry is taken along the Y -axis plane. A moving coordinate system with a velocity corresponding to the laser welding speed is provided to view the scenario as a transient condition. The geometry of the laser welding process used for numerical simulation is schematically shown in Fig. 5 with faces abcd, efgh, and ijkl, respectively. The boundary conditions to describe the

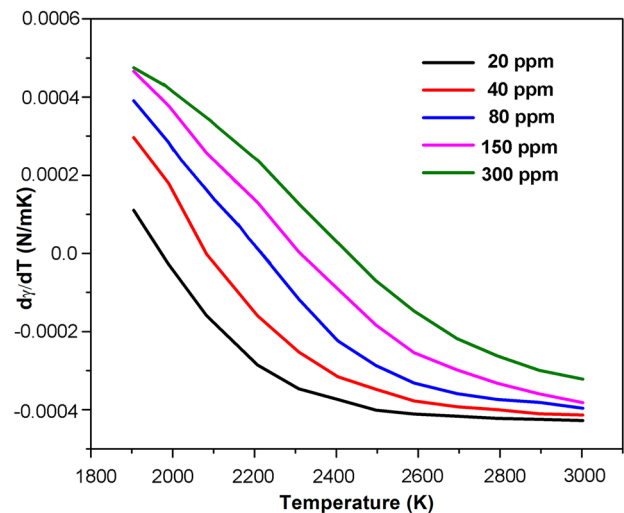


Fig. 4 Effect of TCST (dy/dT) as a function of temperature for varying sulfur content (ppm) in 316 LN SS [44]

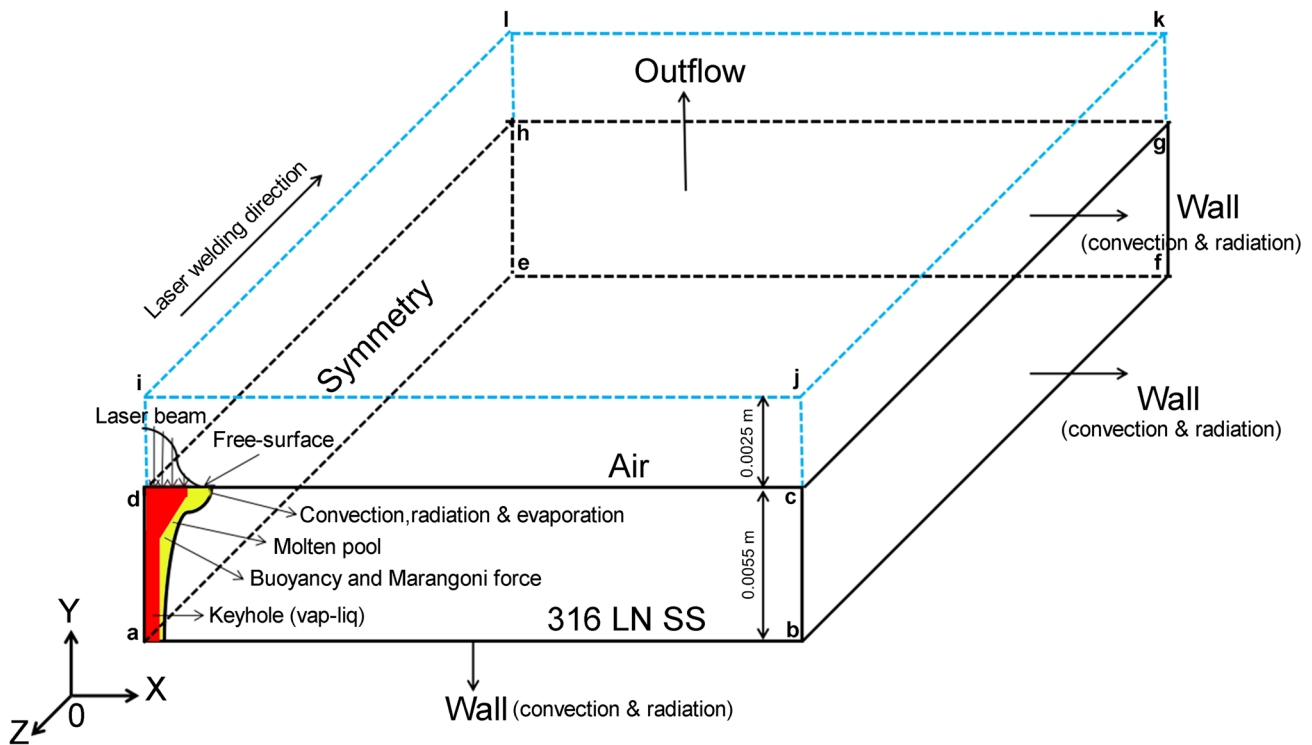


Fig. 5 Geometry model and boundary conditions used for the study

pressure forces, temperature, and velocity fields are given below.

3.4.1 Upper zone boundary condition

The analytical domain is divided into two zones, with a common fluid interface connecting the air and the substrate. The upper zone encompasses the pressure outlet flow condition for the vapor gas evolved during the welding process. Initially, air is considered to be filled in this zone with ambient temperature and atmospheric pressure.

3.4.2 Wall boundary condition

The faces abcd, bfgc, fehg, and abfe of the substrate domain are treated as wall boundary condition accounting heat loss by convection and radiation mainly. The energy condition for heat loss is given as:

$$q_{loss} = q_{conv} + q_{rad} \tag{11}$$

$$q_{conv} = h_{conv}(T - T_0) \tag{12}$$

$$q_{rad} = \sigma \epsilon (T^4 - T_0^4) \tag{13}$$

where h_{conv} , ϵ , and σ are the convection heat transfer coefficient, emissivity of the material, and Stefan Boltzmann constant respectively.

3.4.3 Energy boundary conditions

The energy boundary conditions account for the heat input and heat loss incurred throughout laser melting and keyhole generation by maintaining energy balance on the free surface of the keyhole. The laser source for keyhole generation accounts for energy heat input and heat loss shown as:

$$k \frac{\partial T}{\partial n} = q_{las} - (q_{rad} + q_{conv} + q_{evap}) \tag{14}$$

$$q_{evap} = V_{speed} L_{vap} \tag{15}$$

$$\log(V_{speed}) = 2.52 + \left(6.121 - \frac{18836}{T}\right) - 0.5 \log T \tag{16}$$

V_{speed} is calculated as the vaporization speed for steel which is the function of boiling point given by Hu et al. [45].

3.4.4 Pressure boundary conditions

The depiction of recoil pressure as the dominating force in keyhole creation is one of the most significant pressure boundary conditions used in laser welding. The recoil pressure given by Ge et al. [46] formed due to the deformation of material surface as an effect of evaporation can be stated as:

$$P_{\text{rec}} = 0.54P_o \exp \left\{ \Delta H_{lv} \frac{T - T_{lv}}{RTT_{lv}} \right\} \quad (17)$$

where P_{rec} is the recoil pressure, P_o is the atmospheric pressure, ΔH_{lv} is the latent heat of evaporation, T is the temperature of the weld pool, T_{lv} is the boiling temperature of the material, and R is the universal gas constant.

The recoil pressure is introduced into the computational domain as source term (X , Y , and Z momentum equation) when the temperature of the substrate exceeds the boiling point. The recoil pressure acting vertically to the keyhole wall is decomposed into axial component acting in X , Y , and Z direction. This axial recoil pressure is incorporated by writing an appropriate UDF with n_x , n_y , and n_z as volume fraction gradient components in the numerator and their magnitude of volume fraction in the denominator in the X , Y , and Z direction respectively:

$$P_x = \frac{n_x}{\sqrt{n_x^2 + n_y^2 + n_z^2}}; \quad P_y = \frac{n_y}{\sqrt{n_x^2 + n_y^2 + n_z^2}}; \quad P_z = \frac{n_z}{\sqrt{n_x^2 + n_y^2 + n_z^2}}; \quad (18)$$

The surface tension, acting normal to the free surface fulfilling the pressure condition stated, is expressed as:

$$P = P_{\text{rec}} + P_{\text{surf}} \quad (19)$$

The surface tension force is formulated as a function of surface tension coefficient (γ) and free surface curvature (K) given as:

$$P_{\text{surf}} = \gamma K \quad (20)$$

Here, γ is surface tension coefficient as a function of temperature and sulfur content given by [44]:

$$\gamma = \gamma_m - A(T - T_m) - T\Gamma_s \ln(1 + K_{\text{seg}} S_{\text{cont}}) \quad (21)$$

where γ_m is surface tension of pure iron, and T_m is liquidus temperature.

The free surface curvature is expressed as:

$$K = - \left[\nabla \cdot \left(\frac{\vec{n}}{|\vec{n}|} \right) \right] \quad (22)$$

where \vec{n} is unit vector normal to free surface. In the Fluent solver, effects of the surface tension at free surface are treated using a model via continuum surface stress in the phase interaction module.

3.5 Interfacial tracking by volume of fluid (VOF model)

The VOF multiphase flow framework specifies the tracking mechanism of any fluid throughout CFD analysis. The technique examines the keyhole free surface development. By computing a set of momentum equations, the VOF model calculates the solution for steady or transient settings. The computational domain is divided into two fluid zones, with 316 LN SS in the lower and the air in the top zones. Throughout the computational domain, the volume fraction of each fluid is calculated and projected explicitly, with the volume fraction (F) defined as:

$$\frac{\partial F}{\partial T} + \nabla \cdot (VF) = 0 \quad (23)$$

Whenever a computational cell is thoroughly filled with gas, $F = 0$ is counted, and when a cell is completely filled with liquid, $F = 1$ is computed. A free surface fluid interface is defined when $0 < F < 1$ for the calculated cell.

3.6 Solution method and scheme

Using commercial CFD software ANSYS Fluent V 19.2, the numerical analysis was completed successfully. DESIGN SpaceClaim has been used to construct the geometry that has two separate zones. The analytical domain was 0.015 m long, 0.015 m wide, and 0.008 m tall, including a top void region filled with air enabling free-surface tracking. The geometry was meshed employing

Table 2 316 LN SS material data used in the simulation

Nomenclature	Value
Latent heat of vaporization (J/kg)	6.46×10^6
Molar mass of iron (kg/mol)	0.055845
Gas constant (J/mol-K)	8.314
Vapor temperature (K)	3200
Emissivity-solid, liquid ($\text{W}/\text{m}^2\text{K}^4$)	0.8, 0.4
Thermal expansion coefficient (K^{-1})	1.96×10^{-5}
Gravitational acceleration (m/s^2)	-9.8
Solidus temperature (K)	1670
Liquidus temperature (K)	1730
Surface tension of pure iron (N/m)	1.94
Sulfur content (ppm)	80
Thermal diffusivity (m^2/s)	5.7×10^{-6}

hexahedral controlling cells (1,700,000) adopting elemental sizing with No Bias condition to ensure consistent cell size across the solid domain. Before selecting the appropriate cell size and time step size for the simulation, a mesh sensitivity analysis was done. The numerical model is based on multiphase, in which solid, liquid, and vapor exist in the computational domain due to the sheer complexity of keyhole dynamics. Pressure velocity coupling was employed in conjunction with the SIMPLE scheme and a first-order implicit transient formulation in the solution technique. The conditions were initialized, and the simulation was run on a computer workstation (Intel® Xeon® Processor-48 GB RAM, Core-16, 3.60 GHz, and 6.40 GT/s). The material and physical data of 316LN SS used in the calculation is listed in Table 2.

4 Results and discussion

The heat and molten flow analysis for laser keyhole welding of 316 LN SS for a thickness of 0.0055 m is presented in this research. The anticipated values and patterns of temperature, velocity, and keyhole evolution are detailed in this section. The power intensity for the two volumetric heat sources is coupled by writing UDF code in C language and supplemented as an energy source term. The impact of laser power on the weld depth of penetration is investigated initially on a 0.0055-m-thick 316 LN SS plate by adjusting the laser source parameter settings specified in the conical and cylindrical heat source distribution. The predicted temperature, weld bead characteristics, and weld pool velocity values are examined to estimate the non-dimensional quantities. Next, an optimized laser power identified capable of achieving full penetration is chosen to perform an in-depth study to analyze the weld pool and keyhole development. The compatibility of the hybrid conical-cylindrical heat source model was confirmed by matching it with the experimental result for the optimized laser power.

Table 3 Mesh sensitivity analysis based on weld penetration depth

Sl.no	Mesh size (m)	Depth of penetration (m)	Computational time (s)
1	0.00021	0.0015	0.002
2	0.00018	0.0034	0.004
3	0.00015	0.0041	0.006
4	0.00012	0.0050	0.008
5	0.00009	0.0055	0.010
6	0.00006	0.0055	0.012

4.1 Optimum mesh size and time step study

A mesh sensitivity study is first carried out for the specified welding parameters. Adopting an appropriate time step for the computational domain ensures numerical convergence of the simulation. To assure that the whole physics of the issue is addressed, the time step size is selected such that the laser torch displacement is less than one-tenth of the computational domain. The sensitivity analysis is performed to study the influence of mesh size on the evolution of weld penetration depth, giving a stable result for the calculation time. Table 3 shows the results obtained from the mesh sensitivity analysis. Based on this, the optimum mesh size was chosen as 9×10^{-5} m, and a small-time step (10^{-6} s) was adopted for the simulation.

4.2 Predicted weld pool temperature for various laser power

Temperature profiles for the various laser power show the heat transfer rate interpreted by the hybrid conical-cylindrical heat source model, as shown in Fig. 6. The temperature rises rapidly as the laser beam traverses over the plate's surface, melting the material. The weld pool temperature raises as the laser power advances from 1 to 3.5 kW, as shown by thermal isotherms, and reaches a peak value returning it to a quasi-steady state. When viewed from the top, the thermal isotherm seems to be elliptic in shape and bunched ahead of the laser source due to more significant temperature gradients. In contrast, it looks less dense at the back of the laser source due to lower temperature gradients. The keyhole depth is minimal at low power, but it becomes more profound as the recoil pressure rises due to greater energy density, finally achieving full penetration. The peak temperature was found to reach 3521 K for 3.5 kW laser power, more than the boiling temperature of the material. As a result, the heat transmission rate is determined by the laser source power, resulting in a deeper weld. The optimum laser power for achieving full penetration is predicted to be 3 kW. The predicted weld pool width and depth of penetration are inferred from the solidification/melting contour plots indicating the laser weld melted region (1730 K melting temperature for 316 LN SS) displayed in Fig. 7. With a rise in laser power density, the weld pool width and penetration depth increase, finally reaching full penetration for a power of 3.5 kW. However, the influence of power on weld width is not so sensitive compared to the depth of penetration.

4.3 Predicted weld pool velocity for various laser power

The predicted fluid velocities for varying laser power is illustrated in 3D (Fig. 8), showing the effect on molten pool shape.

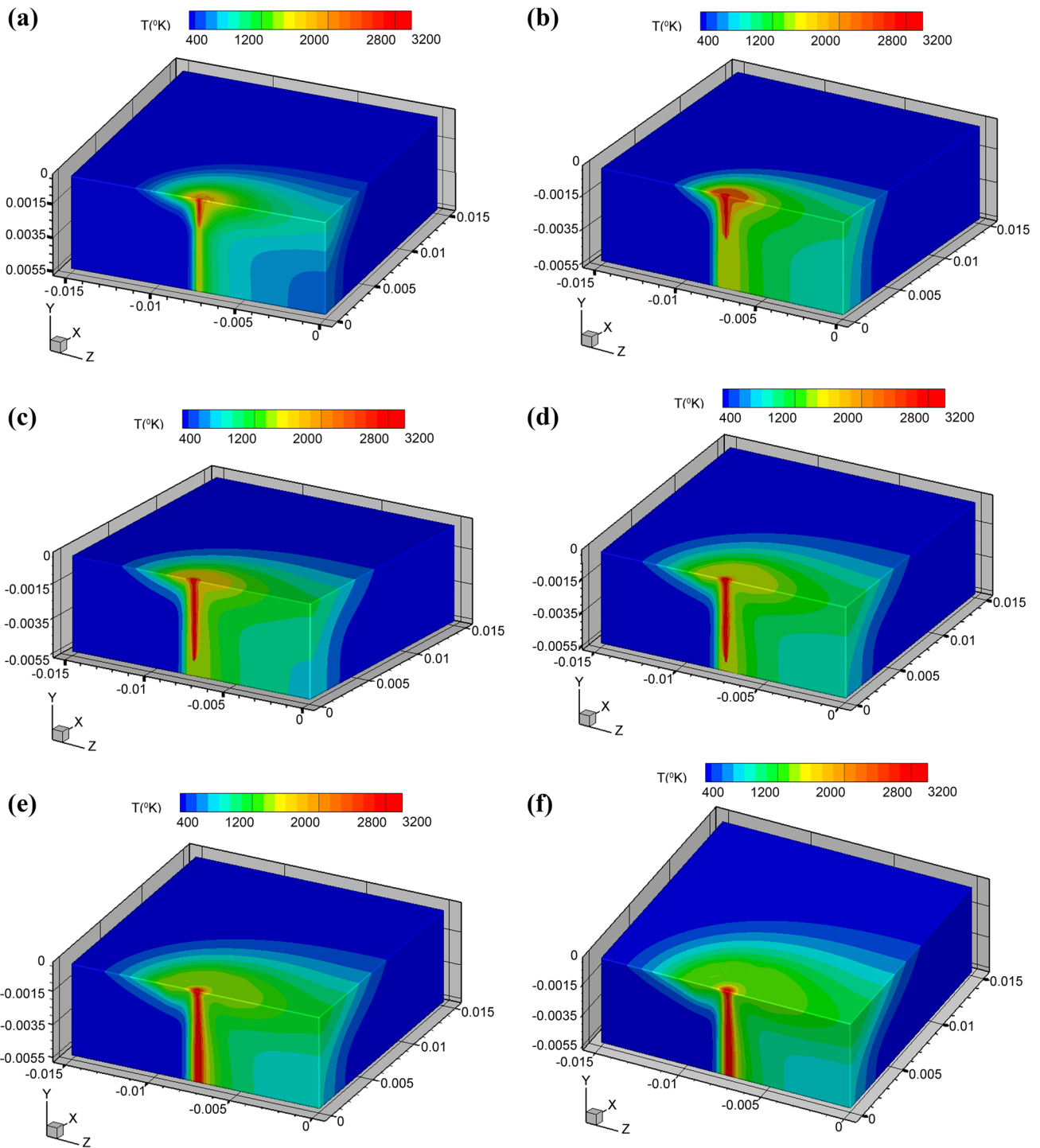


Fig. 6 Simulation results of the weld pool temperature in a three-dimensional view for different laser power. **a** 1.0 kW. **b** 1.5 kW. **c** 2.0 kW. **d** 2.5 kW. **e** 3.0 kW. **f** 3.5 kW

The arrows indicate the velocity distribution pattern of the molten pool along with their magnitude. The molten pool seems to be affected by the TCST value due to the presence of surface-active element (sulfur), with radially outward circulation flows, indicating that convection is the primary heat

transfer method as seen in Fig. 8e (X–Y plane). From Fig. 4, the critical temperature for the weld metal containing 80 ppm sulfur is approximately 2275 K. The TCST remains negative since the weld center temperature is ahead of this value, and outward convection flow is generated. Near to the keyhole,

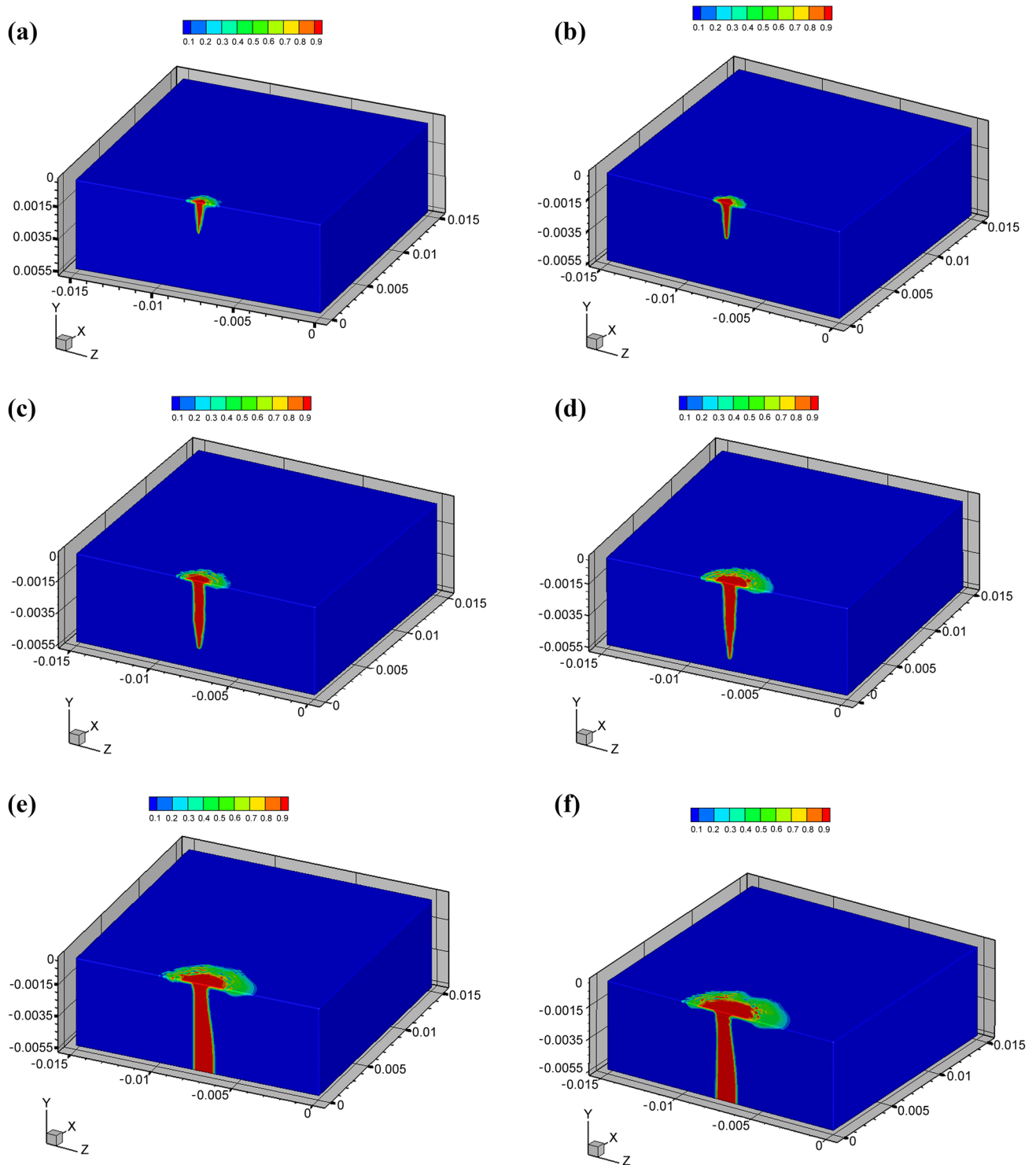


Fig. 7 Simulation results of the weld pool liquid contour in a three-dimensional view for different laser power. **a** 1.0 kW. **b** 1.5 kW. **c** 2.0 kW. **d** 2.5 kW. **e** 3.0 kW. **f** 3.5 kW

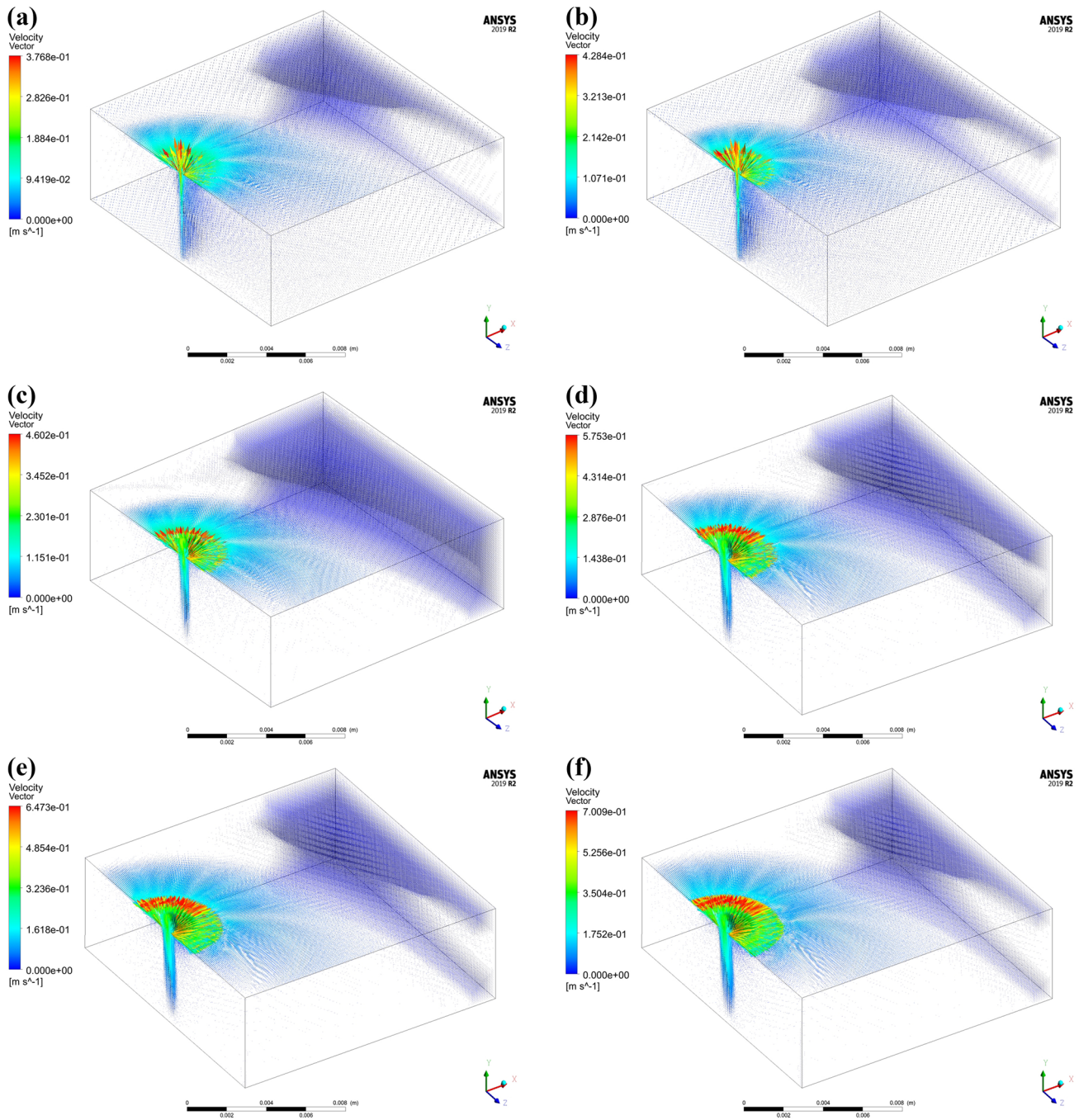


Fig. 8 Simulation results of the weld pool velocity in a three-dimensional view for different laser power. **a** 1.0 kW. **b** 1.5 kW. **c** 2.0 kW. **d** 2.5 kW. **e** 3.0 kW. **f** 3.5 kW

high-temperature gradient exists, and hence, Marangoni convection is more vigorous, as seen in Fig. 8e, f. The Marangoni convection weakens as it moves away from the keyhole, and fluid velocity drops. The heat transfer is more effective due to the fluid flow owing to the rise in laser power, thus increasing the magnitude and elongation of weld pool length.

The computed values of maximum weld pool temperature, velocity, and weld bead attribute (bead width, depth, and length) for varying laser power are shown in Table 4. The volume of molten metal increases owing to the rise in the laser power. Consequently, there is increase in the weld pool velocity and weld penetration for higher power density.

Table 4 Predicted weld bead dimensions for various power

Laser power (kW)	Heat input (kJ/mm)	Maximum temperature (K)	Melt pool velocity (m/s)	Melt pool width (m)	Melt pool depth (m)	Characteristic length (m)
1.0	0.060	2078	0.376	0.0008	0.0018	0.0009
1.5	0.100	2399	0.428	0.0010	0.0025	0.0011
2.0	0.133	2631	0.460	0.0013	0.0040	0.0014
2.5	0.166	2831	0.575	0.0016	0.0050	0.0016
3.0	0.200	3310	0.647	0.0020	0.0055	0.0019
3.5	0.233	3521	0.700	0.0022	0.0055	0.0021

4.4 Non-dimensional analysis

The numerical investigation results provide a better understanding of the physical process of laser welding since there is a reasonable agreement between the predicted and experimental results. The predicted thermal profile and velocity fields can offer crucial information on heat transfer, solidification, and cooling features that affect the overall weld quality by computing non-dimensional numbers such as Peclet number, Marangoni number, and Fourier number.

4.4.1 Marangoni number

The Marangoni number is a dimensionless quantity often used to assess surface tension effects upon the weld pool interface due to the molten liquid flow resulting from the surface tension temperature gradient. The influence of Marangoni stress on the weld pool velocity is essentially what the number signifies. It may be represented mathematically as:

$$Ma = \frac{L_{width} \Delta T}{\alpha \mu} \left(-\frac{d\gamma}{dT} \right) \quad (24)$$

where the characteristic length (L_{width}) is taken as the half-width of weld pool, ΔT is the change in temperature from liquidus to solidus, α is the thermal diffusivity, μ is the dynamic viscosity, and $\left(\frac{d\gamma}{dT} \right)$ is TCST.

Table 5 Marangoni and Peclet numbers of the weld pool

Laser power (kW)	Heat input (kJ/mm)	Marangoni number	Peclet number
1.0	0.066	1813	26.38
1.5	0.100	4050	37.54
2.0	0.133	6940	52.45
2.5	0.166	10,320	80.70
3.0	0.200	18,222	113.50
3.5	0.233	22,623	135.08

4.4.2 Peclet number

The Peclet number determines either conduction or convection is the dominant mode of heat transmission. Compared to conduction, where the value is substantially less than 1, large Peclet numbers (more than 1) usually contribute to the convection mode of heat transmission. The velocity levels at various places have an impact on the Peclet number. The expression is specified as:

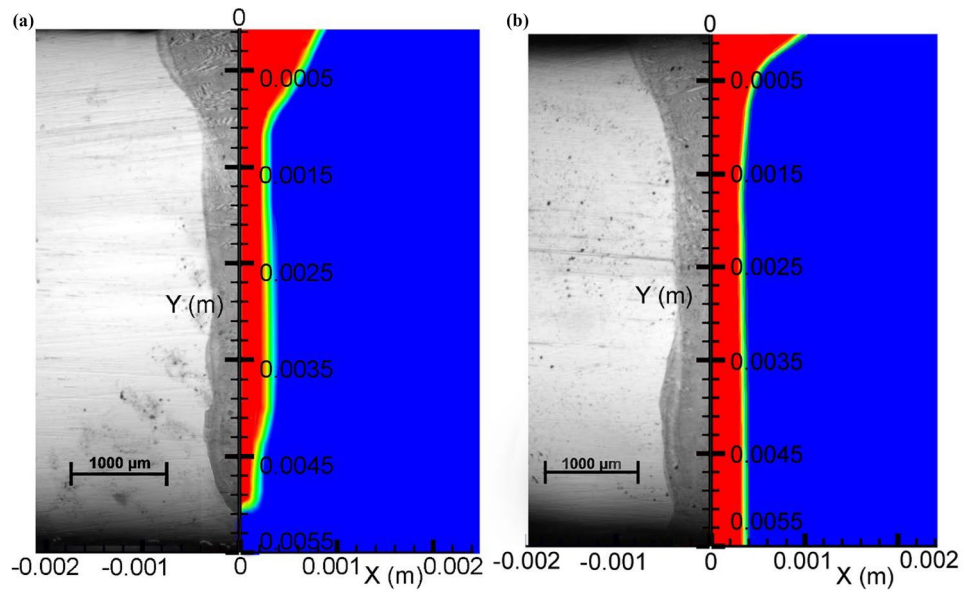
$$Pe = \frac{L_{width} u_{max}}{\alpha} \quad (25)$$

The computed dimensionless numbers are listed in Table 5. For all the studied cases, the weld pool characteristic length and velocity of the molten metal increases owing to the increase in heat input. From the analysis, the Marangoni number gets higher as the heat input increases signifying a stronger convection current. The Marangoni convection becomes crucial for the laser power of more than 2 kW ($Ma > 10^5$). This effect can contribute to increase in the weld penetration depth. Also, the increase in Marangoni value indicates a higher velocity in the molten pool, which in turn affects the mode of heat transfer defined by Peclet number. The Peclet number value computed within the molten pool is much larger than 1 for various heat input. These high values show that the principal mechanism of the heat transfer throughout the melt pool seems to be convective heat transfer. Therefore, the role of convective heat transfer is more significant during weld pool development. An increase in the Marangoni number leads to a higher Peclet value and more prominent convective heat transfer within the molten pool.

4.5 Predicted vs. experimental trails

The current study emphasizes to achieve full depth of penetration in 0.0055-m-thick 316 LN plate by selecting an optimum power level. Initially, simulation was carried out by varying the power levels to visualize the weld depth of penetration. In order to validate the predicted results, bead-on-plate trail experiments were conducted by selecting two

Fig. 9 Experimental and predicted weld bead cross-section comparison for laser power. **a** 2.5 kW. **b** 3.5 kW



power levels (2.5 kW and 3.5 kW) to verify the amount of weld penetration depth. After the trials, the weld bead cross-section were compared with the predicted results as shown in Fig. 9. The actual weld penetration depths for 2.5 kW and 3.5 kW were measured to be 0.0051 m and 0.0055 m respectively. Hence, a good agreement was found between the predicted and experimental weld bead geometry and dimension. The correlated values are listed in Table 6. Since the computed result displayed maximum depth of penetration for laser power more than 3 kW, an optimum laser power of 3.3 kW was selected to perform the laser square butt welding.

4.6 Temperature and velocity field profile for optimized welding power

The required amount of power to produce a through-thickness laser weld is identified as 3 kW. A detailed CFD study is presented to gain information about the molten pool development, keyhole evolution, and cooling phenomenon with an optimized laser power of 3.3 kW. The computed results are analyzed to understand the overall laser weld properties of 316 LN SS.

The initial forces acting during weld pool formation are mainly surface tension and Marangoni force. When the weld pool surpasses the critical surface tension temperature, the

molten metal starts flowing from the keyhole center towards the edge and then flows downward, forming a vortex due to the Marangoni force. Once the material exceeds the evaporation point, recoil pressure depresses the weld pool surface and eventually, the penetration depth increases with time. The weld pool temperature reaches a maximum value of 3390 K, having a maximum pool velocity of 0.65 m/s, as shown in Fig. 10.

The keyhole temperature which is above the materials’ evaporation range is consistent with the previous report investigated by Pang et al. [47] while the temperature of the molten pool is within the liquidus range of the material. The temperature of the weld pool attains a maximum value and, at last, reaches a steady-state depth.

4.7 Keyhole evolution for optimized laser power

The keyhole evolution during the laser welding at different time steps is displayed in Fig. 11 (X–Y plane). Here, the volume of metal in the liquid phase is considered filled (bottom), whereas the surrounding air and metallic vapor are taken as gaseous phases with an initial value of 0 (top). For tracking the gas–liquid interface evolution, a sharp interface modeling technique is applied embedded in the software. In the beginning, the laser beam interacts with the substrate and weld pool formation begins owing to the melting

Table 6 Comparison of weld size-measured and predicted

Weld bead attributes	2.5 kW			3.5 kW		
	Measured	Predicted	Error %	Measured	Predicted	Error %
Penetration depth (m)	0.005	0.0048	4	0.0055	0.0055	0
bead width top (m)	0.0019	0.0018	5.2	0.002	0.0022	–10
bead width bottom (m)	0.00038	0.0004	–5.2	0.0009	0.0008	11

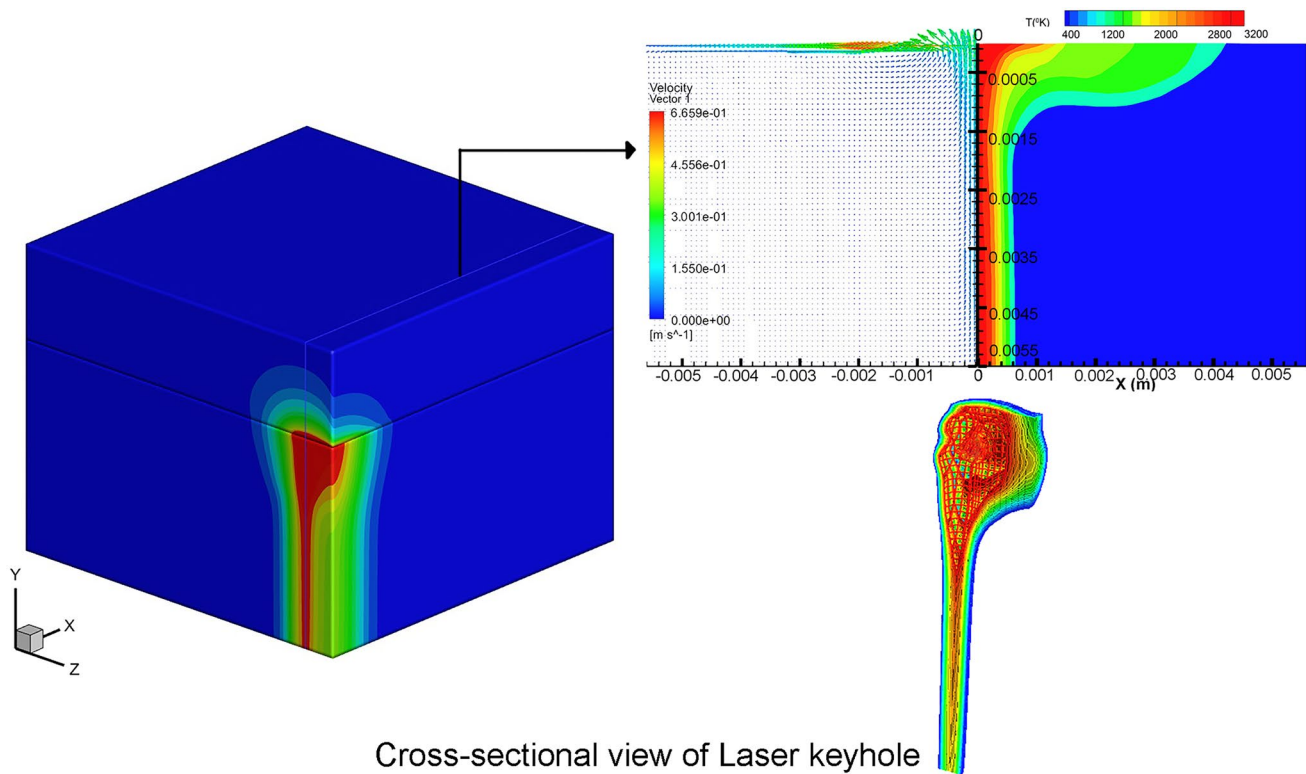


Fig. 10 Temperature distribution and velocity field for 3.3-kW laser power in 3D

phenomenon (conduction mode) at time less than 3 ms. As the weld temperature increases due to the intense laser heat, evaporation process occurs once the irradiated region surpasses the boiling temperature of the material, pushing the molten metal out, thereby creating a slight depression along with the interface seen in Fig. 11b. The recoil force opposing the metal vapor ejection plays a dominant role by exerting downward pressure, forming a shallow keyhole at 5 ms. Recoil force acting during the laser welding aids in moving the molten metal from the top to the bottom side of the keyhole when the welding time approaches 10 ms. The increase in weld temperature further causes the keyhole to gain penetration depth by pulling the molten metal upwards and ultimately forming full penetration. There is an interaction between molten flow generated by the Marangoni force and the recoil pressure resulting in deformation along the vapor–liquid interface, as shown in Fig. 11e.

The velocity distribution of the metallic vapor generated along the gas–liquid boundary is shown in Fig. 12 for two different time steps. In this study, an estimation of the expelled metal vapor velocity during the keyhole generation is presented since experimental observations were limited in the current study while performing the laser welding. Once the material surpasses the evaporation temperature, metallic vapor starts expelling from the cavity formed due to intense laser power density at time

5 ms shown in Fig. 12a. The major portion of the vapor originates from the keyhole as shown. The direction of the vapor flow is towards the outflow boundary. As the keyhole forms, the recoil pressure in contact with the vapor plume drives down along the keyhole wall forming a circulation loop. There is variation in the velocity values around the keyhole, as the value is dependent on the process parameters. A maximum velocity around 60 m/s is observed from the velocity scale, although it is not visible from the figure. This may be present in very small regions. However, an average value of about 15–30 m/s is found at the upper portion of the keyhole under atmospheric condition. The claimed value is approximate to previously published literature data of Wang et al. [48] The variation of recoil pressure for the temperature from the current study is plotted in Fig. 13. The maximum pressure attained for the weld peak temperature is around 133 kPa, as seen in Fig. 14, displaying the contour and velocity fields of recoil vapor pressure. The high-pressure and low-pressure regions can be seen viewed at the opening and middle portion of the keyhole. Also, low-pressure regions can be found along the edge of the keyhole. The average value of vapor pressure has been reported by Tenner et al. [49] and Zhang et al. [50] of 111 kPa and 123 kPa respectively. The recoil pressure velocity direction is acting downward as seen in Fig. 15b, reported in previous work by Pang et al. [47].

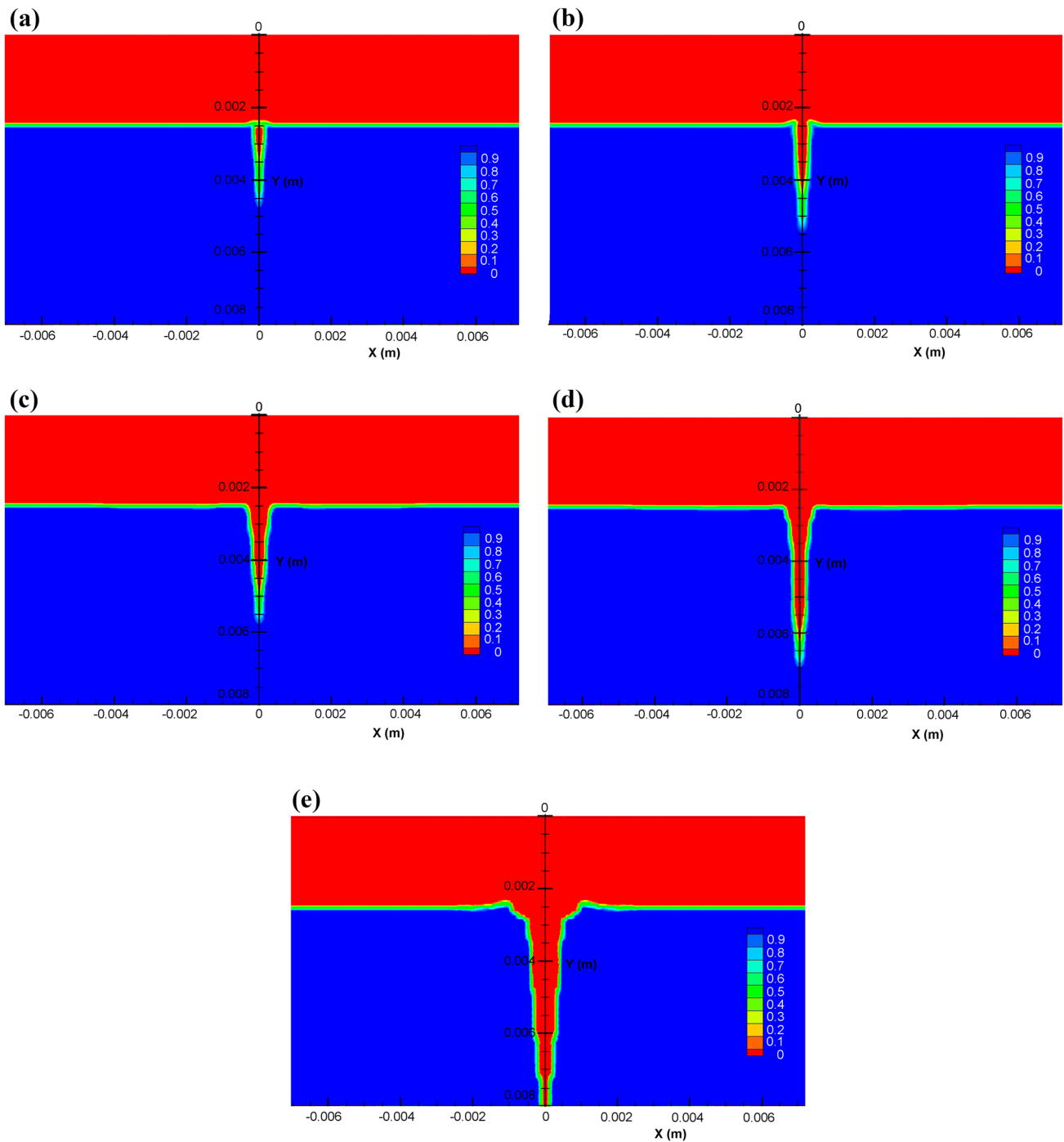


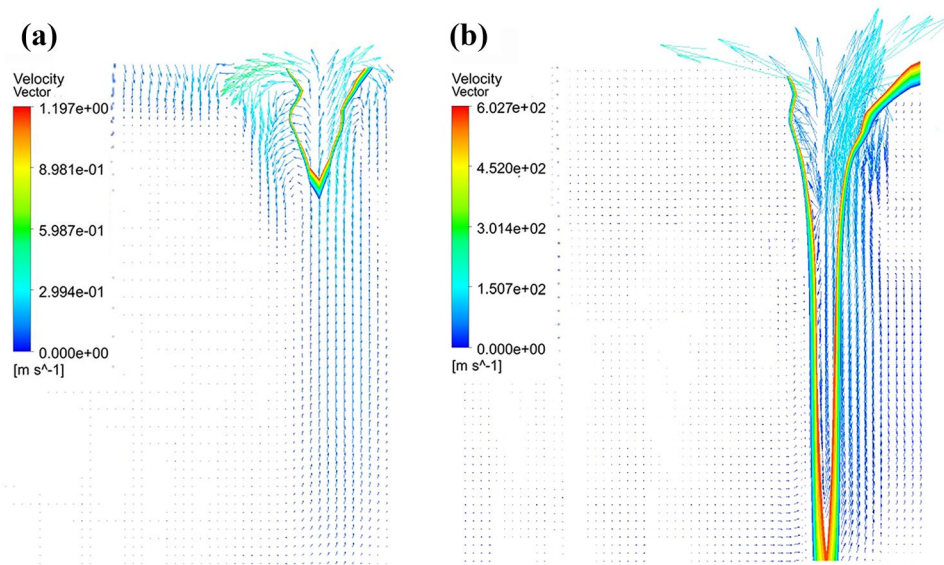
Fig. 11 Keyhole evolution with time (ms) during optimized laser welding. **a** $t=3$ ms. **b** $t=5$ ms. **c** $t=7$ ms. **d** $t=8.5$ ms. **e** $t=10$ ms

4.8 Predicted cooling rate for secondary dendrite arm spacing calculation

The cooling rate (CR) data can be used to examine the solidification morphology and fusion zone characteristics of the welding processes. When laser welding, a rapid cooling rate of 10^4 to 10^6°C s^{-1} is typically induced, resulting in finer dendritic structure after solidification

and lesser SDAS. The columnar dendritic structure is revealed by electrolytically etching the weld cross-section by an equal amount of water and nitric acid as shown in Fig. 15a. The dendritic structure grows finer for a high cooling rate and vice versa. The SDAS is a measure of the ratio of length of the primary dendrite arm to the number of secondary dendrite arm present throughout the length as displayed in Fig. 15c. The SDAS

Fig. 12 Predicted vapor velocity for 316 LN SS at **a** $t=5$ ms. **b** $t=10$ ms



mean value reported in this study have been made from the measurements taken at different locations across the weld zone. The average value of SDAS were measured to be $2.23 \pm 0.13 \mu\text{m}$.

The solidification cooling rate of the weld fusion zone can be extracted from the 3D model once the process attains quasi-steady state. At any location along the weld centerline, the cooling rate is calculated by:

$$\frac{\partial T}{\partial t} = \left| \frac{T_s - T_l}{t_s - t_l} \right| \quad (26)$$

where T_s and T_l correspond to the solidus and liquidus temperature of the material reached at t_s and t_l respectively. As a result, computed cooling rates (Ks^{-1}) may be utilized to calculate the SDAS (μm) for the 316 LN SS. There exists a linear relation between the parameters of log SDAS and log

CR whose values were determined experimentally by Elmer et al. [51] for stainless steel. The relation given below was employed for the 316 LN SS to predict the SDAS as investigated by Mukherjee et al. [52]:

$$SDAS = 25(CR)^{-0.28} \quad (27)$$

The abovementioned methodology is applied in this study to calculate the cooling rate of the fusion zone. The predicted thermal cycle of the weld fusion zone for the optimized welding condition can be observed in Fig. 16. The cooling rate calculated from the Eq. is found to be in the order of $0.69 \times 10^4 \text{ K/s}$. The SDAS value from the above calculation is estimated to be $2.10 \mu\text{m}$. The predicted dendritic spacing was found to be relatively closer with the actual value implying the accuracy of the numerical model.

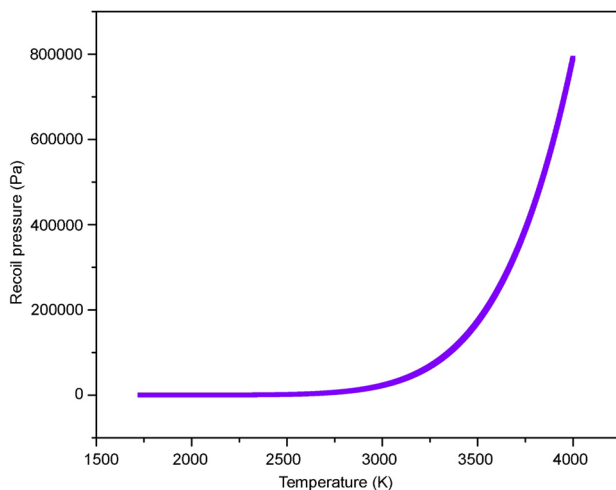
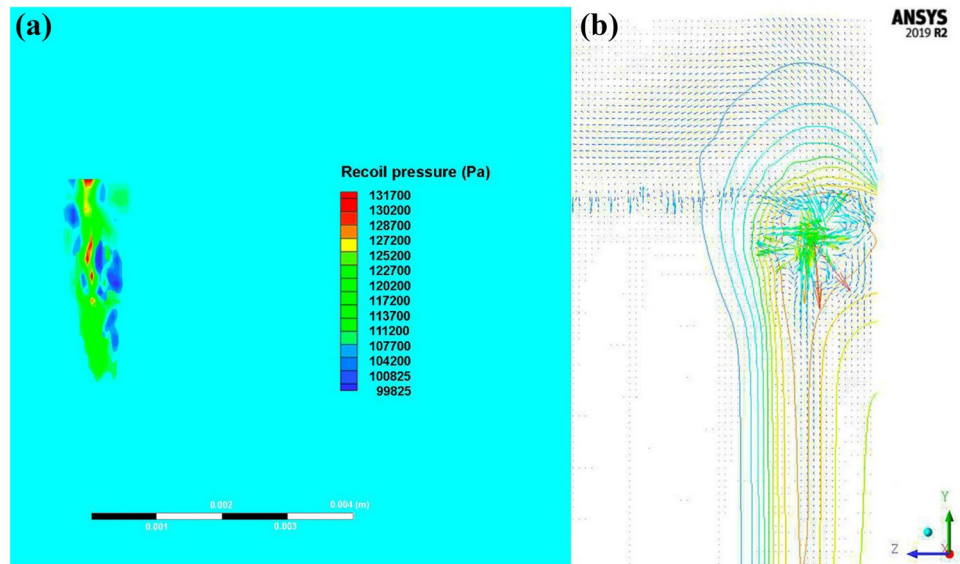


Fig. 13 Recoil pressure as a function of weld temperature

4.9 Verification of the numerical model

The numerical model's reliability is established by conducting a laser welding experiment with an optimized welding parameter of 3.3 kW, giving full penetration. To validate the predicted results, the experimentally obtained laser weld bead shape is compared. The weld fusion zone boundary is defined by the liquidus temperature of 316 LN SS, depicting the area of melt contour. The morphology of the weld bead cross-section shown in the X–Y plane (front view) of the simulation is in good accordance with the experimental weld bead shape. The weld's top and bottom bead dimensions in the predicted results are identical to those obtained in the experiment with minimum error given in Table 7. The comparison of simulated weld bead geometry to the experimental weld cross-section is shown in Fig. 17.

Fig. 14 Recoil pressure. **a** Pressure contour. **b** Velocity field



In addition, thermal distribution patterns recorded using TC's tack welded at four locations were matched to the peak temperature field values acquired during CFD simulation.

The TC 1, TC 2, TC 3, and TC 4 were positioned along the transverse direction, maintaining a 0.001 m, 0.002 m, 0.003 m, and 0.004 m, respectively, away from the weld

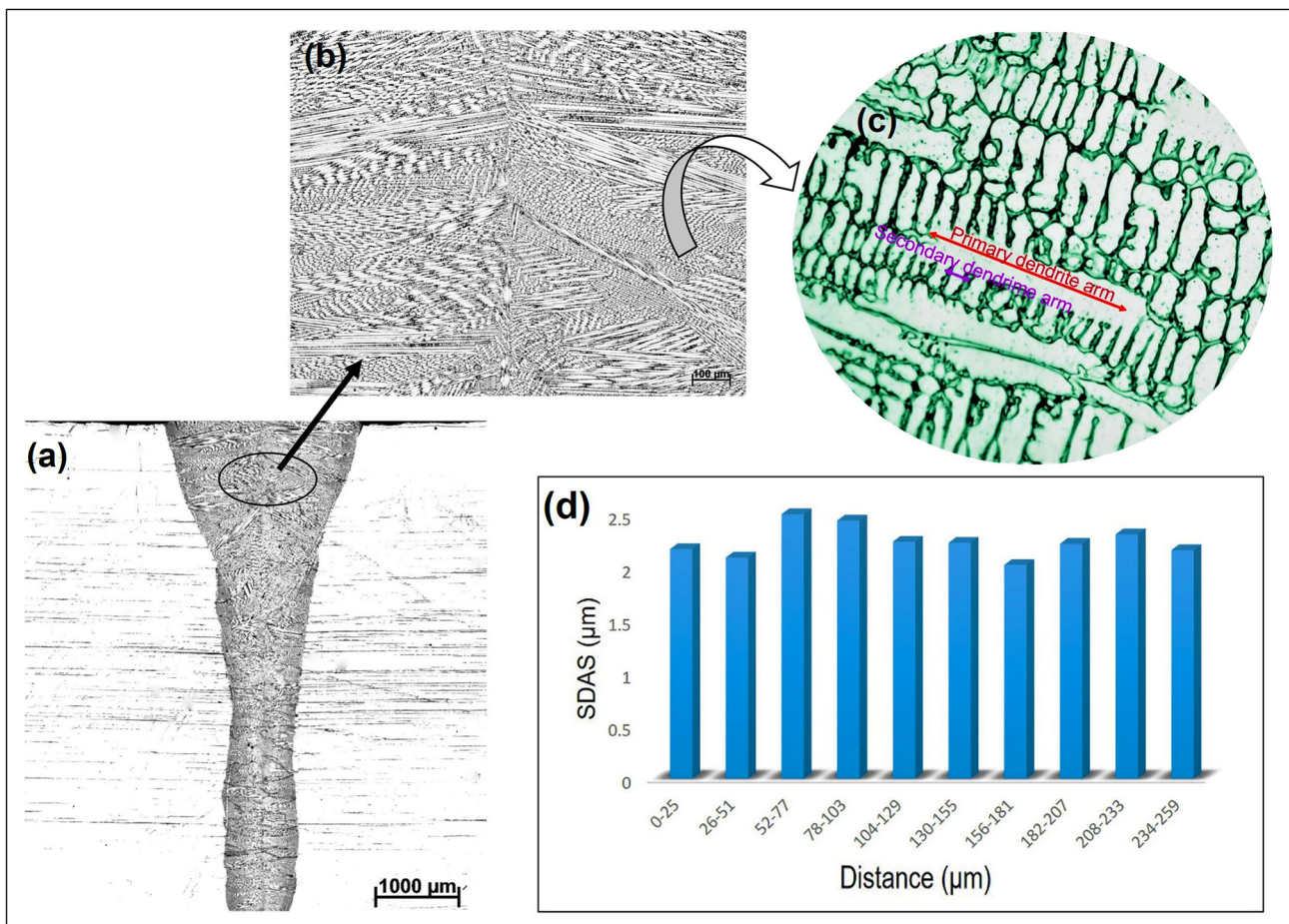
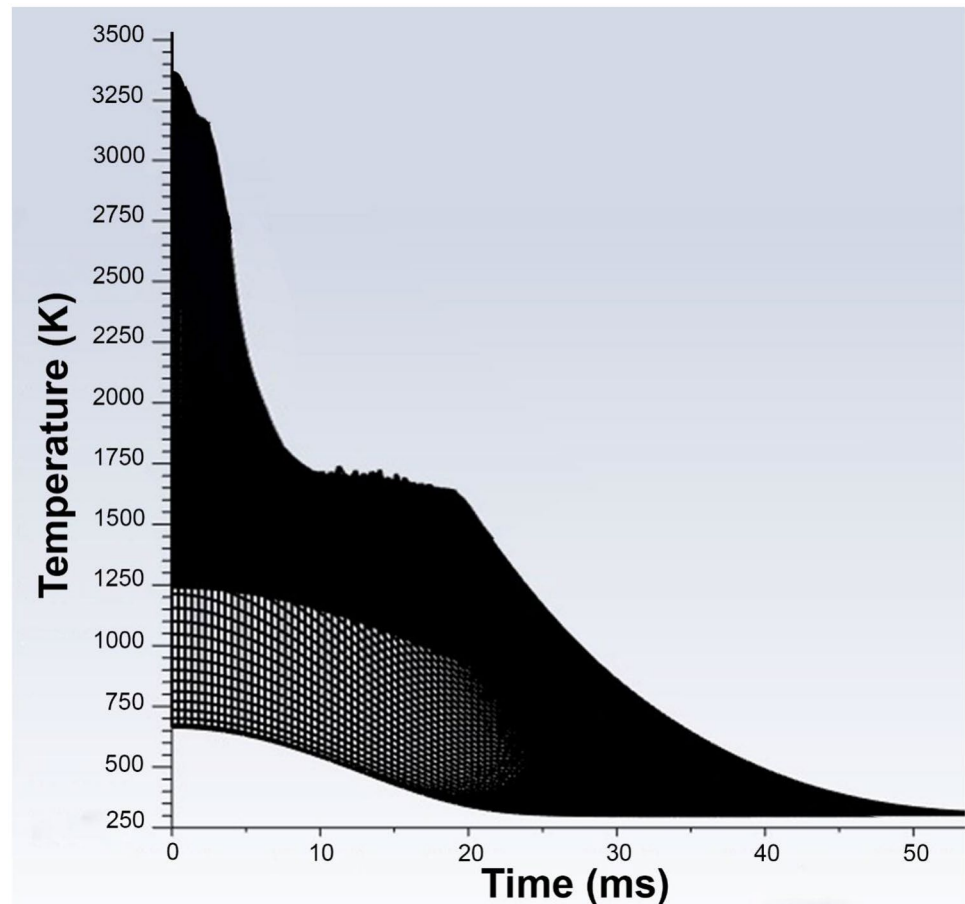


Fig. 15 Laser 316 LN SS weld dendrite arm spacing. **a**, **b** Fusion zone microstructure. **c** SDAS zoomed image (1000× magnification). **d** SDAS value measured across fusion zone

Fig. 16 Predicted weld thermal cycle for optimized welding condition



fusion line. A data acquisition unit connected with the TC measured the peak surface temperature in degree Kelvin. The thermal distribution data were tracked only for TC 2, TC 3, and TC 4. The temperature data in the close proximity of the fusion line (TC 1—0.001 m) was cut off instantly during laser welding. The maximum surface temperatures obtained from TC placed at 0.002 m, 0.003 m, and 0.004 m are 1150 K, 885 K, and 580 K, which is in close agreement with the predicted temperature values achieved in the same spot measured adjacent to the weld centerline shown in Fig. 18.

The entire study focused on CFD simulation of weld pool development and keyhole evolution using hybrid conical-cylindrical heat source model for laser welding of 316 LN SS. In our earlier study [25], we reported that

Table 7 Predicted weld size and measured size comparison

Weld bead attributes	Measured	Predicted	Error %
Depth of penetration (m)	0.0055	0.0055	0
Weld bead width top (m)	0.0024	0.0022	8.3
Weld bead width bottom(m)	0.0009	0.0008	11.0

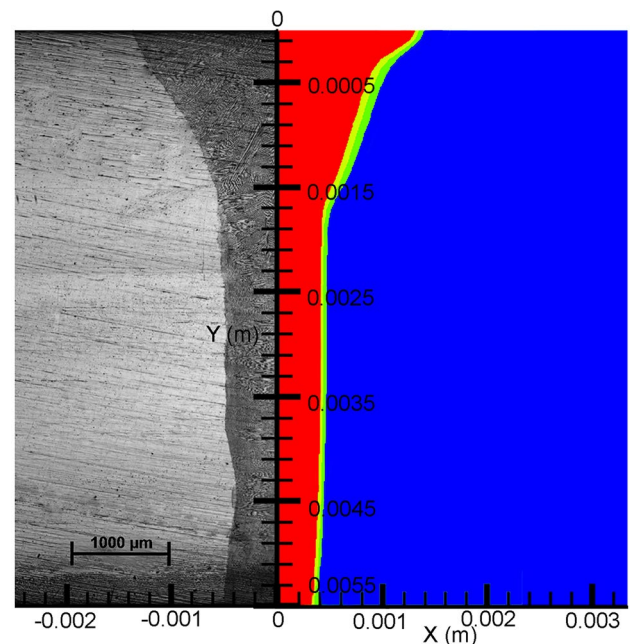


Fig. 17 Comparison of experimental (left side) and predicted (right side) weld fusion zone shapes in front view (cross-section)

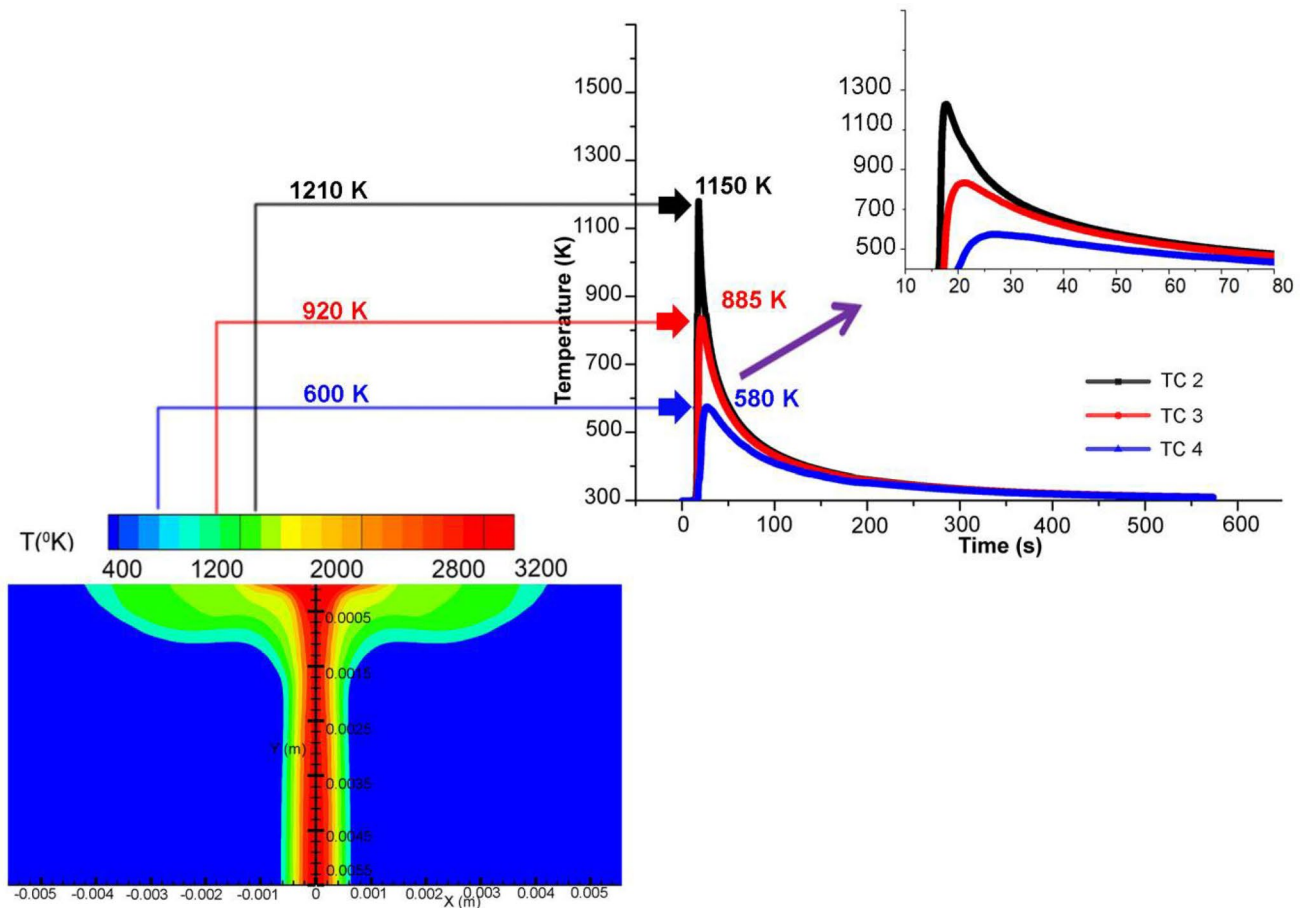


Fig. 18 Comparison of experimental and predicted peak thermal values positioned at 0.002 m, 0.003 m, and 0.005 m from weld centerline

conical-cylindrical heat source exhibited good agreement with the measured weld bead dimensions and the temperature during simulation of laser welding of 316 LN stainless steel. The optimized hybrid conical-cylindrical heat source could simulate the actual weld bead shape and size, and predict weld pool temperature, molten flow velocity, keyhole profile, vapor velocity, and weld cooling rate fairly well for the laser welding of stainless steel in the present study. The model also provided more insight on the weld pool evolution during laser welding accurately. The numerically computed weld cooling rate using the CFD model gives fair calculation of secondary dendrite arm spacing across the fusion zone when compared with the measured actual value.

5 Conclusions

In this study, a 3D transient numerical model based on the CFD multiphase analysis has been investigated to evaluate the heat transfer, weld pool flow, keyhole formation, and

fusion zone attributes during the laser welding of 316 LN SS. The detailed conclusions drawn from the developed model are as follows:

1. The hybrid conical-cylindrical heat source model is recommended as a noble and reliable choice for the CFD simulation of laser keyhole welding based on the resemblance with the experimental weld pool shape and dimensions.
2. The variation in laser power caused changes in the value of weld peak temperature and weld bead traits. The optimum level of laser power to produce full penetration in 0.0055-m-thick plate was identified to be 3 kW which is in agreement with the experimental result.
3. The depth of penetration and bead width of the weld metal are influenced by the increase in laser power, implying that TCST has an effect on the thermal-fluid flow mechanism. The strength of the Marangoni convection is superior due to high thermal gradient ahead of the keyhole and gradually weakens away from the center.

4. The temperature distribution, velocity field, and the keyhole evolution for the optimized laser weld bead are demonstrated. The evolution of metallic vapor and recoil pressure is reported during the laser welding of 316 LN SS.
5. The numerically computed SDAS value obtained from the weld cooling rate is compared to the equivalent value measured from the solidification structure. Both the computed and actual result were found to be satisfactory.
6. The predicted weld peak temperatures at 0.002 m, 0.003 m, and 0.004 m away from the weld center are found to be reasonable with the TC measured peak values, thus proving the validity of the numerical model.

Author contribution Anoop K Unni: methodology, software, investigation, data analysis and interpretation, writing—original draft. Vasudevan Muthukumaran: conceptualization, supervision, writing, review and editing.

Data availability Not applicable.

Code availability The numerical analyses have been performed using commercially licensed software ANSYS Fluent V 19.2 with specific user-defined function code written in C language that is made available by the authors under request.

Declarations

Ethics approval The present manuscript contains an original research; it has not been published elsewhere, it has not been submitted simultaneously for publication elsewhere, and publication has been approved by the co-author.

Consent to participate Not applicable.

Consent for publication The present paper does not require any consent to publish since all the figures, tables, and text are original.

Conflict of interest The authors declare no competing interests.

References

1. Wang S, Zhang M, Wu H, Yang B (2016) Study on the dynamic recrystallization model and mechanism of nuclear grade 316LN austenitic stainless steel. *Mater Charact* 118:92–101. <https://doi.org/10.1016/j.matchar.2016.05.015>
2. Kumar JG, Chowdary M, Ganesan V (2010) High temperature design curves for high nitrogen grades of 316LN stainless steel. *Nucl Eng Des* 240:1363–1370. <https://doi.org/10.1016/j.nucengdes.2010.02.038>
3. Bachmann M, Gumenyuk A, Rethmeier M (2016) Welding with high-power lasers: Trends and developments. *Phys Procedia* 83:15–25. <https://doi.org/10.1016/j.phpro.2016.08.003>
4. Mackwood AP, Crafer RC (2005) Thermal modelling of laser welding and related processes: a literature review. *Opt Laser Technol* 37:99–115. <https://doi.org/10.1016/j.optlastec.2004.02.017>
5. Xia P, Yan F, Kong F et al (2014) Prediction of weld shape for fiber laser keyhole welding based on finite element analysis. *Int J Adv Manuf Technol* 75:363–372. <https://doi.org/10.1007/s00170-014-6129-4>
6. Hozorbakhsh A, Hamdi M, Sarhan AADM et al (2019) CFD modelling of weld pool formation and solidification in a laser micro-welding process. *Int Commun Heat Mass Transf* 101:58–69. <https://doi.org/10.1016/j.icheatmasstransfer.2019.01.001>
7. Rosenthal D (1946) The theory of moving source of heat and its application to metal transfer. *ASME Trans* 43:849–866
8. Rykalin NN (1974) Es. *Weld World, Le Soudage Dans Le Monde* 12
9. Steen WM, Dowden J, Davis M, Kapadia P (1988) A point and line source model of laser keyhole welding. *J Phys D Appl Phys* 21:1255. <https://doi.org/10.1088/0022-3727/21/8/002>
10. Davis M, Kapadia P, Dowden J (1986) Modelling the fluid flow in laser beam welding. *Weld J (Miami, Fla)* 65:167-s-174-s
11. Mazumder J, Steen WM (1980) Heat transfer model for cw laser material processing. *J Appl Phys* 51:941. <https://doi.org/10.1063/1.327672>
12. Li P, Fan Y, Zhang C et al (2018) Research on heat source model and weld profile for fiber laser welding of A304 stainless steel thin sheet. *Adv Mater Sci Eng*. <https://doi.org/10.1155/2018/5895027>
13. Lorin S, Julia M, Rikard S, Kristina W (2022) A new heat source model for keyhole mode laser welding. *J Comput Inf Sci Eng J* 22(1):011004. <https://doi.org/10.1115/1.4051122>
14. Attar MA, Ghoreishi M, Beiranvand ZM (2020) Prediction of weld geometry, temperature contour and strain distribution in disk laser welding of dissimilar joining between copper & 304 stainless steel. *Optik (Stuttg)* 219:165288. <https://doi.org/10.1016/j.ijleo.2020.165288>
15. Tsirkas SA, Papanikos P, Kermanidis T (2003) Numerical simulation of the laser welding process in butt-joint specimens. *J Mater Process Technol* 134:59–69. [https://doi.org/10.1016/S0924-0136\(02\)00921-4](https://doi.org/10.1016/S0924-0136(02)00921-4)
16. Shanmugam NS, Buvanashakaran G, Sankaranarayanan K, Manonmani K (2009) Some studies on temperature profiles in AISI 304 stainless steel sheet during laser beam welding using FE simulation. *Int J Adv Manuf Technol* 43:78–94. <https://doi.org/10.1007/s00170-008-1685-0>
17. Li X, Lu F, Cui H, Tang X, Wu Y (2014) Numerical modeling on the formation process of keyhole-induced porosity for laser welding steel with T-joint. *Int J Adv Manuf Technol* 72:241–254. <https://doi.org/10.1007/s00170-014-5609-x>
18. Jiang P, Wang C, Zhou Q et al (2016) Optimization of laser welding process parameters of stainless steel 316L using FEM, Kriging and NSGA-II. *Adv Eng Softw* 99:147–160. <https://doi.org/10.1016/j.advengsoft.2016.06.006>
19. Li L, Peng G, Wang J et al (2019) Numerical and experimental study on keyhole and melt flow dynamics during laser welding of aluminium alloys under subatmospheric pressures. *Int J Heat Mass Transf* 133:812–826. <https://doi.org/10.1016/j.ijheatmasstransfer.2018.12.165>
20. Faraji AH, Goodarzi M, Seyedein SH et al (2015) Numerical modeling of heat transfer and fluid flow in hybrid laser–TIG welding of aluminum alloy AA6082. *Int J Adv Manuf Technol*. <https://doi.org/10.1007/s00170-014-6589-6>
21. Wang R, Lei Y, Shi Y (2011) Numerical simulation of transient temperature field during laser keyhole welding of 304 stainless steel sheet. *Opt Laser Technol* 43:870–873. <https://doi.org/10.1016/j.optlastec.2010.10.007>
22. Zhan X, Mi G, Zhang Q, Wei Y, Ou W (2017) The hourglass-like heat source model and its application for laser beam welding of 6 mm thickness 1060 steel. *Int J Adv Manuf Technol* 88:2537–2546. <https://doi.org/10.1007/s00170-016-8797-8>
23. Chukkan JR, Vasudevan M, Muthukumaran S et al (2015) Simulation of laser butt welding of AISI 316L stainless steel sheet using

- various heat sources and experimental validation. *J Mater Process Technol* 219:48–59. <https://doi.org/10.1016/j.jmatprotec.2014.12.008>
24. Evdokimov A, Springer K, Doynov N (2017) Heat source model for laser beam welding of steel-aluminum lap joints. *Int J Adv Manuf Technol* 93:709–716. <https://doi.org/10.1007/s00170-017-0569-6>
 25. Unni AK, Vasudevan M (2021) Determination of heat source model for simulating full penetration laser welding of 316 LN stainless steel by computational fluid dynamics. *Mater Today Proc* 45:4465–4471. <https://doi.org/10.1016/j.matpr.2020.12.842>
 26. Artinov A, Bachmann M, Rethmeier M (2018) Equivalent heat source approach in a 3D transient heat transfer simulation of full-penetration high power laser beam welding of thick metal plates. *Int J Heat Mass Transf* 122:1003–1013. <https://doi.org/10.1016/j.ijheatmasstransfer.2018.02.058>
 27. Lee JY, Ko SH, Farson DF, Yoo CD (2002) Mechanism of keyhole formation and stability in stationary laser welding. *J Phys D Appl Phys* 35:1570. <https://doi.org/10.1088/0022-3727/35/13/320>
 28. Roñda J, Siwek A (2011) Modelling of laser welding process in the phase of keyhole formation. *Arch Civ Mech Eng* 11:739–752. [https://doi.org/10.1016/s1644-9665\(12\)60113-7](https://doi.org/10.1016/s1644-9665(12)60113-7)
 29. Zhao H, Niu W, Zhang B et al (2011) Modelling of keyhole dynamics and porosity formation considering the adaptive keyhole shape and three-phase coupling during deep-penetration laser welding. *J Phys D Appl Phys* 44:485302. <https://doi.org/10.1088/0022-3727/44/48/485302>
 30. Feng Y, Gao X, Zhang Y, Peng C, Gui X, Sun Y, Xiao X (2021) Simulation and experiment for dynamics of laser welding keyhole and molten pool at different penetration status. *Int J Adv Manuf Technol* 112:2301–2312. <https://doi.org/10.1007/s00170-020-06489-y>
 31. Le TN, Lo YL (2019) Effects of sulfur concentration and Marangoni convection on melt-pool formation in transition mode of selective laser melting process. *Mater Des* 179:107866. <https://doi.org/10.1016/j.matdes.2019.107866>
 32. Unni AK, Vasudevan M (2021) Numerical simulation of the influence of oxygen content on the weld pool depth during activated TIG welding. *Int J Adv Manuf Technol* 112:467–489. <https://doi.org/10.1007/s00170-020-06343-1>
 33. Mills KC, Keene BJ (1990) Factors affecting variable weld penetration. *Int Mater Rev* 35:185–216. <https://doi.org/10.1179/095066090790323966>
 34. Rai R, Elmer JW, Palmer TA, Debroy T (2007) Heat transfer and fluid flow during keyhole mode laser welding of tantalum, Ti-6Al-4V, 304L stainless steel and vanadium. *J Phys D Appl Phys* 40:5753. <https://doi.org/10.1088/0022-3727/40/18/037>
 35. Ribic B, Tsukamoto S, Rai R, DebRoy T (2011) Role of surface-active elements during keyhole-mode laser welding. *J Phys D Appl Phys* 44:485203. <https://doi.org/10.1088/0022-3727/44/48/485203>
 36. Hozoorbakhsh A, Ismail MIS, Sarhan AADM (2016) An investigation of heat transfer and fluid flow on laser micro-welding upon the thin stainless steel sheet (SUS304) using computational fluid dynamics (CFD). *Int Commun Heat Mass Transf* 75:328–340. <https://doi.org/10.1016/j.icheatmasstransfer.2016.05.008>
 37. Geng S, Jiang P, Shao X et al (2020) Heat transfer and fluid flow and their effects on the solidification microstructure in full-penetration laser welding of aluminum sheet. *J Mater Sci Technol* 46:50–63. <https://doi.org/10.1016/j.jmst.2019.10.027>
 38. Das D, Pratihari DK, Roy GG (2018) Cooling rate predictions and its correlation with grain characteristics during electron beam welding of stainless steel. *Int J Adv Manuf Technol* 97:2241–2254. <https://doi.org/10.1007/s00170-018-2095-6>
 39. Zhao C, Kwakernaak C, Pan Y, Richardson I, Saldi Z, Kenjeres S, Kleijn C (2010) The effect of oxygen on transitional marangoni flow in laser spot welding. *Acta Mater* 58:6345–6357. <https://doi.org/10.1016/j.actamat.2010.07.056>
 40. Chakraborty N (2009) The effects of turbulence on molten pool transport during melting and solidification processes in continuous conduction mode laser welding of copper–nickel dissimilar couple. *Appl Therm Eng* 29:3618–3631. <https://doi.org/10.1016/j.applthermaleng.2009.06.018>
 41. Kidess A, Kenjeres S, Righolt BW, Kleijn CR (2016) Marangoni driven turbulence in high energy surface melting processes. *Int J Therm Sci* 104:412–422. <https://doi.org/10.1016/j.ijthermalsci.2016.01.015>
 42. Faraji AH, Carmine M, Giuseppe B, Francesco C, Luigi B (2021) Numerical modeling of fluid flow, heat, and mass transfer for similar and dissimilar laser welding of Ti-6Al-4V and Inconel 718. *Int J Adv Manuf Technol* 114:899–914. <https://doi.org/10.1007/s00170-021-06868-z>
 43. Ai Y, Jiang P, Shao X et al (2017) The prediction of the whole weld in fiber laser keyhole welding based on numerical simulation. *Appl Therm Eng*. <https://doi.org/10.1016/j.applthermaleng.2016.11.050>
 44. Sahoo P, Debroy T, McNallan MJ (1988) Surface tension of binary metal-surface active solute systems under conditions relevant to welding metallurgy. *Metall Trans B*. <https://doi.org/10.1007/BF02657748>
 45. Hu B, Hu S, Shen J, Li Y (2015) Modeling of keyhole dynamics and analysis of energy absorption efficiency based on Fresnel law during deep-penetration laser spot welding. *Comput Mater Sci*. <https://doi.org/10.1016/j.commatsci.2014.09.031>
 46. Ge W, Fuh JYH, Na SJ (2021) Numerical modelling of keyhole formation in selective laser melting of Ti6Al4V. *J Manuf Process*. <https://doi.org/10.1016/j.jmapro.2021.01.005>
 47. Pang S, Chen X, Zhou J et al (2015) 3D transient multiphase model for keyhole, vapor plume, and weld pool dynamics in laser welding including the ambient pressure effect. *Opt Lasers Eng*. <https://doi.org/10.1016/j.optlaseng.2015.05.003>
 48. Wang J, Wang C, Meng X et al (2012) Study on the periodic oscillation of plasma/vapour induced during high power fibre laser penetration welding. *Opt Laser Technol*. <https://doi.org/10.1016/j.optlastec.2011.05.020>
 49. Tenner F, Brock C, Gürtler FJ et al (2014) Experimental and numerical analysis of gas dynamics in the keyhole during laser metal welding. In: *Physics Procedia*
 50. Zhang L, Zhang J, Zhang G et al (2011) An investigation on the effects of side assisting gas flow and metallic vapour jet on the stability of keyhole and molten pool during laser full-penetration welding. *J Phys D Appl Phys* 44:135201. <https://doi.org/10.1088/0022-3727/44/13/135201>
 51. Elmer JW, Allen SM, Eagar TW (1989) Microstructural development during solidification of stainless steel alloys. *Metall Mater Trans A* 20:2117–2131. <https://doi.org/10.1007/BF02650298>
 52. Mukherjee T, Manvatkar V, De A, DebRoy T (2017) Dimensionless numbers in additive manufacturing. *J Appl Phys* 121:064904. <https://doi.org/10.1063/1.4976006>

Publisher's Note Springer Nature remains neutral with regard to jurisdictional claims in published maps and institutional affiliations.

Springer Nature or its licensor holds exclusive rights to this article under a publishing agreement with the author(s) or other rightsholder(s); author self-archiving of the accepted manuscript version of this article is solely governed by the terms of such publishing agreement and applicable law.